J. Fluid Mech. (2005), *vol.* 534, *pp.* 351–401.
doi:10.1017/S0022112005004507 Printed in the United Kingdom

Numerical and experimental investigation of flow and scour around a circular pile

By ANDREAS ROULUND[1], B. MUTLU SUMER[1], JØRGEN FREDSØE[1] AND JESS MICHELSEN[2]

[1]Technical University of Denmark, MEK, Coastal, Maritime and Structural Engineering Section (formerly ISVA) Building 403, DK-2800 Kgs. Lyngby, Denmark

[2]Technical University of Denmark, MEK, Fluid Mechanics Section, Building 403, DK-2800 Kgs. Lyngby, Denmark

(Received 6 August 2003 and in revised form 6 December 2004)

The flow around a vertical circular pile exposed to a steady current is studied numerically and experimentally. The numerical model is a three-dimensional model. The model validation was achieved against new experimental data (which include two-component laser-Doppler anemometry (LDA) flow measurements and the hot-film bed shear stress measurements, and reported in the present paper) and the data of others, and a k–ω turbulence model was used for closure. The model does not have a free-surface facility and therefore is applicable only to cases where the Froude number is small ($Fr < O(0.2)$). The flow model was used to study the horseshoe vortex and lee-wake vortex flow processes around the pile. The influence on the horseshoe vortex of three parameters, namely the boundary-layer thickness, the Reynolds number and the bed roughness, was investigated. In the latter investigation, the steady solution of the model was chosen. A study of the influence of the unsteady solution on the previously mentioned flow processes was also carried out. The ranges of the parameters covered in the numerical simulations are: The boundary-layer-thickness-to-pile-diameter ratio is varied from 2×10^{-2} to 10^2, the pile Reynolds number from 10^2 to 2×10^6, and the pile diameter-to-roughness ratio from 2 to about 10^3. The amplification of the bed shear stress around the pile (including the areas under the horseshoe vortex and the lee-wake region) was obtained for various values of the previously mentioned parameters. The steady-state flow model was coupled with a morphologic model to calculate scour around a vertical circular pile exposed to a steady current in the case of non-cohesive sediment. The morphologic model includes (i) a two-dimensional bed load sediment-transport description, and (ii) a description of surface-layer sand slides for bed slopes exceeding the angle of repose. The results show that the present numerical simulation captures all the main features of the scour process. The equilibrium scour depth obtained from the simulation agrees well with the experiments for the upstream scour hole. Some discrepancy (up to 30 %) was observed, however, for the downstream scour hole. The calculations show that the amplification of the bed shear stress around the pile in the equilibrium state of the scour process is reduced considerably with respect to that experienced at the initial stage where the bed is plane.

1. Introduction

When a vertical circular pile is placed on the bed in a steady current, the flow will undergo substantial changes (figure 1): (i) a horseshoe vortex is formed in front of the pile; (ii) a vortex flow pattern (usually in the form of vortex shedding) is formed

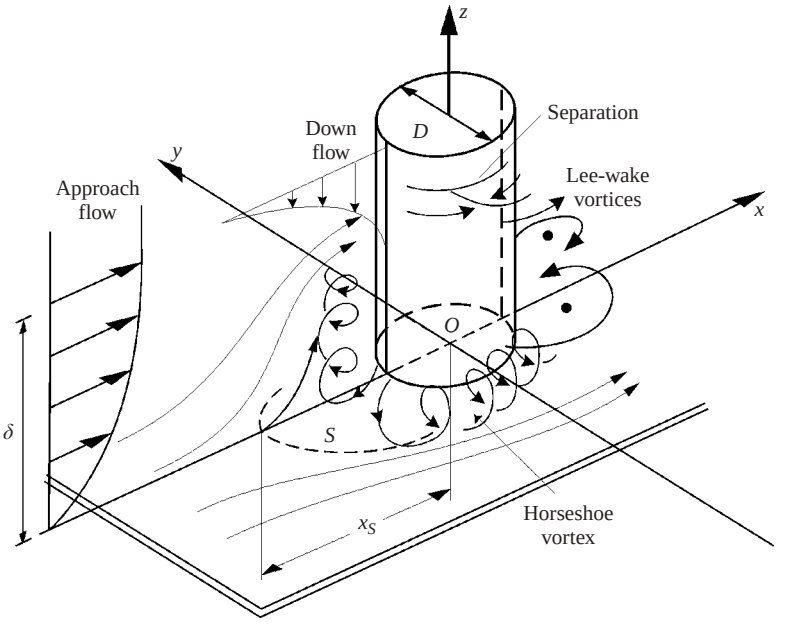

FIGURE 1. Definition sketch.

at the lee-side of the pile; and (iii) the streamlines contract at the sides of the pile. In addition, there exists a downflow as a consequence of flow deceleration in front of the pile. If the bed is erodible, the overall effect of these changes is generally to increase the sediment transport, resulting in local scour around the pile. Extensive scour around the pile may reduce its stability, thus leading to its failure. Incidentally, both the terms pile and pier are used invariably in the literature (mostly the term pile in the marine-engineering literature and pier in the hydraulic-engineering literature). We will use the term pile hereinafter to be consistent with our earlier work (see e.g. Sumer & Fredsøe 2002).

Scour around piles in steady currents has been investigated extensively (particularly in the context of scour at bridge piers). Reviews of the subject can be found in Breusers, Nicollet & Shen (1977), Dargahi (1982), Breusers & Raudkivi (1991), Richardson & Davies (1995), Dey (1997*a*, *b*), Hoffmans & Verheij (1997), Raudkivi (1998), Whitehouse (1998), Melville & Coleman (2000) and Sumer & Fredsøe (2002).

While much has been written on the subject of flow and scour around piles in steady currents, comparatively few studies have been presented of the three-dimensional numerical modelling of these processes.

Briley & McDonald (1981) made Navier–Stokes (N-S) computations of a laminar steady horseshoe vortex at the junction between an elliptic strut and a flat plate. Using a three-dimensional incompressible N-S code, Kwak *et al.* (1986) computed the laminar steady junction flow. Deng & Piquet (1992) studied the three-dimensional turbulent flow about an airfoil/flat-plate junction, where the main features of the horseshoe vortex are captured by the study. An iterative fully decoupled technique was applied to the Reynolds-averaged N-S equations in this study. A comprehensive review of the work up to the early 1990s was given by Deng & Piquet (1992).

Three-dimensional numerical calculations of flow around a vertical wall-mounted cylinder have also been carried out in order to study the scour.

Olsen & Melaaen (1993) and Olsen & Kjellesvig (1998) were the first to undertake such calculations in conjunction with the three-dimensional modelling of scour around a circular pile. The bed material was *cohesionless sediment*. In Olsen & Melaaen (1993), the flow was calculated using the steady-state N-S equations on a three-dimensional non-orthogonal grid. The Reynolds stress terms were solved using the k–ε turbulence model. Sediment transport equations (with an equation for bed concentration) were incorporated into the model for scour calculations. Only the clear-water scour case was simulated in the calculations (i.e. the sediment transport in the undisturbed case was nil). Comparison was made with experimentally measured scour patterns, and good agreement was obtained. The study appears to produce the horseshoe vortex in front of the cylinder (Olsen & Melaaen 1993, figure 4). Olsen & Kjellesvig (1998) continued the work reported in Olsen & Melaaen (1993). They essentially used the same formulation as in Olsen & Mallaen (1993). The investigation was not limited to the initial stage of scour (which was the case in Olsen & Melaaen 1993); rather, the entire scour process was simulated. The scour was in the clear-water regime (Olsen, personal communication, 2002). The scour depth obtained in the calculations agreed well with the scour depth obtained from empirical formulae.

Richardson & Panchang (1998) also made three-dimensional calculations of the flow around a vertical circular cylinder. The calculations were made for three cases: one with a rigid plane bed, the second with an intermediate 'frozen' scour hole and the third one with an equilibrium 'frozen' scour hole. The latter scour holes were 'copies' of those measured in Melville & Raudkivi's (1977) clear-water experiment. Turbulence closure was achieved through a number of advanced schemes, including Prandtl's mixing-length theory, the eddy-viscosity model, the two-equation k–ε model, and the renormalized group (RNG) theory. As in the work of Olsen and co-workers, the steady solution of flow was obtained, and the horseshoe vortex was resolved. No scour simulation (with a live bed) was undertaken.

Tseng, Yen & Song (2000) were the third group of workers to make three-dimensional calculations of the flow around a vertical wall-mounted cylinder (exposed to a steady current). They used large-eddy simulation (LES). In the calculations, both the horseshoe vortex and the vortex shedding were resolved. The model results were validated against the results of Dargahi's (1989) experiments. Subsequently, simulation runs were undertaken to study various properties of the three-dimensional flow around both circular and square cylinders. Although the implications of the flow for scour processes were discussed, no scour simulation was undertaken.

Chen (2002) employed a Reynolds-averaged N-S method to predict scour in an array of piers in a side-by-side arrangement (complex pier configuration). The bed material was *cohesive sediment*, and the scour rate is assumed to vary linearly with the bed shear stress. The latter made it relatively easy to calculate the bed morphology. The horseshoe vortices were resolved in front of the piers. Calculations were performed for two kinds of complex pier configurations: (i) for a model scale complex rectangular pier configuration and (ii) for a prototype complex circular pier configuration. This was to illustrate the general capabilities of the method for prediction of combined global and local pier scour.

The research presented in the present paper was stimulated by the work of Olsen & Melaaen (1993) and Olsen & Kjellesvig (1998). They were the only ones to simulate the actual scour process in cohesionless sediment; but the scour was in the clear-water regime whereas the present investigation deals with a live bed.

With a flow/scour model used in the present study, processes responsible for scour could be studied numerically (particularly for conditions that cannot be achieved, or

are difficult to achieve, in the laboratory), addressing questions such as: (i) What is the effect of the pile Reynolds number on the horseshoe vortex, one of the key elements of the scour process? (ii) Likewise, what is the effect of the thickness of the approaching boundary layer? (iii) Similarly, what is the effect of the bed roughness? (iv) What is the 'amplification' in the bed shear stress around the pile (another important element regarding the scour process), and what is the effect of the aforementioned parameters on this amplification? (v) What is the influence of the unsteady flow solution (where the vortex shedding is resolved) on the horseshoe vortex? (vi) What is the bed shear stress inside a live scour hole and how does it evolve as the scour process continues? etc.

The purpose of the present investigation is to study the flow and live-bed scour around a circular pile exposed to a steady current in cohesionless sediment. To this end, a three-dimensional flow code, EllipSys3D, has been employed to simulate the flow, both with a rigid plane bed and with a sediment bed undergoing scour; and the flow code together with a morphodynamic model have been implemented to simulate the actual live-bed scour process around the pile. The numerical model has enabled us to study the flow and scour processes, particularly in relation to the issues referred to in the preceding paragraph.

2. Hydrodynamic model

2.1. *Governing equations*

The three-dimensional general purpose flow solver, EllipSys3D, was used to calculate the flow. It is an incompressible general purpose N-S solver. It is a multiblock finite-volume numerical model that solves the incompressible Reynolds-averaged N-S equations

$$\frac{\partial \rho U_i}{\partial t} + \frac{\partial \rho U_i U_j}{\partial x_j} = -\frac{\partial p}{\partial x_i} + \frac{\partial}{\partial x_j}\left[(\mu + \mu_T)\left(\frac{\partial U_i}{\partial x_j} + \frac{\partial U_j}{\partial x_i}\right)\right], \tag{1}$$

in which U_i is the ith component of velocity; t is the time; x_j are the Cartesian coordinates; ρ is the fluid density; p is the dynamic pressure; μ is the viscosity; and μ_T is the eddy viscosity, calculated by a two-equation eddy-viscosity type turbulence model, as detailed in the following section. EllipSys3D has been developed at the Risø National Laboratory, Denmark and at the Technical University of Denmark, Department of Fluid Mechanics. (One of the authors of the present paper (J. M.) has been involved in the development of this flow code.) A variety of turbulence models are available. The model is under constant development. The basic principles of the model have been described in Michelsen (1992) and Sørensen (1995). The following web address can be consulted for further information: http://www.risoe.dk/vea-aed/numwind/flowsolver.htm.

In the present study, two kinds of hydrodynamic calculation have been performed: (i) steady-state-flow calculations; and (ii) unsteady-flow calculations.

In the steady-state-flow calculations, the SIMPLE algorithm (Patankar 1980) is used. In this algorithm, the pressure field is calculated and the velocity field is corrected so that the continuity equation,

$$\frac{\partial \rho}{\partial t} + \frac{\partial (\rho U_j)}{\partial x_j} = 0, \tag{2}$$

is satisfied in an iterative manner. By under-relaxation of the correction to the velocity field, the unsteady components of the flow are suppressed.

Although the majority of the present study involved steady-state flow calculations, some unsteady-flow calculations have also been performed. In the unsteady-flow calculations, the PISO algorithm (Issa 1986), an algorithm similar to SIMPLE, is used. In this algorithm, no under-relaxation is applied, and the unsteady components of the flow are maintained.

The HYBRID scheme of Spalding (1972) is used for calculations of the convective terms in the momentum equations (equation (1)). It may be noted that HYBRID has the form of a first-order upwind difference scheme in regions where the flow is dominated by the convective term in (1). In regions where the diffusion is dominating, i.e. at separation points, the HYBRID scheme has the form of a second-order central difference scheme. HYBRID has proved to be very stable, a feature that is important for scour calculations.

Finally, it may be noted that EllipSys3D has some distinct features. Most prominently, EllipSys3D relies on multigrid solution techniques for the elliptic equations. This makes the solver very fast. Another property is that the code structure is 'open and transparent', alleviating inclusion of even complex auxiliary models, such as, for instance, the morphology model as in the present application. A third property is that the so-called Rhie–Chow momentum interpolation used in EllipSys has been corrected to make it consistent for unsteady-flow computations (as reported in Shen, Michelsen & Sørensen 2001). Other than these features, most of EllipSys3D (including the previously mentioned algorithms) relies on techniques that have been proved in previous work. The numerical code has been used in various engineering problems (particularly in wind engineering); the following publications can be cited: Shen *et al.* (2001, 2003, 2004), Sørensen, Michelsen & Schreck (2002) and Johansen *et al.* (2002).

2.2. *Turbulence model*

The k–ω model (Wilcox 1993) has been selected as the turbulence model because of its better performance (Menter 1993; Wilcox 1993) in the case of boundary-layer flows with a strong adverse pressure gradient, as will be detailed in the following paragraphs.

There are three versions of the k–ω model in the literature: (i) the original k–ω model, which is due to Wilcox; (ii) the k–ω, BSL (baseline) model; and (iii) the k–ω, SST (shear-stress transport) model. The latter two models were developed by Menter (1993) to improve Wilcox's original model so that an even higher sensitivity could be obtained for adverse-pressure-gradient flows.

Menter (1993) made an extensive comparison between (i) the classic k–ε model; (ii) the original k–ω model; (iii) the k–ω, BSL model; and (iv) the k–ω, SST model for various well-documented flows. The tested flows were, among others, two kinds of adverse-pressure-gradient flow (one having a very strong adverse pressure gradient, so strong that separation occurs); the backward-facing-step flow; and the flow past a NACA 4412 airfoil at an angle of attack near maximum lift condition. The latter two flows also have substantial adverse-pressure-gradient effects. The main conclusion from this inter-comparison exercise was that the k–ω, SST model gave the most accurate results while the k–ε model did not yield results as accurate as the other three for the tested adverse-pressure-gradient flow cases. For this reason, the k–ω, SST model has been chosen for the present application in which there is a strong adverse pressure effect (see the pressure distribution in figure 18(*b*), which will be discussed later), the effect responsible for the formation of the horseshoe vortex in front of the pile. The quantity k in the k–ω model is the turbulent kinetic energy

and ω the specific dissipation of turbulent kinetic energy, as will be detailed in the following paragraphs.

Now, the k–ω model is essentially based on two equations, one equation for k, and the other equation for ω:

$$\frac{\partial \rho k}{\partial t} + \frac{\partial \rho U_j k}{\partial x_j} - \frac{\partial}{\partial x_j}\left[(\mu + \sigma_k \mu_T)\frac{\partial k}{\partial x_j}\right] = \tau_{ij}\frac{\partial U_i}{\partial x_j} - \beta^* \rho k \omega, \tag{3}$$

$$\frac{\partial \rho \omega}{\partial t} + \frac{\partial \rho U_j \omega}{\partial x_j} - \frac{\partial}{\partial x_j}\left[(\mu + \sigma_\omega \mu_T)\frac{\partial \omega}{\partial x_j}\right] = \frac{\gamma}{\nu_T}\tau_{ij}\frac{\partial U_i}{\partial x_j} - \beta \rho \omega^2 + 2\rho(1 - F_1)\frac{\sigma_{\omega 2}}{\omega}\frac{\partial k}{\partial x_j}\frac{\partial \omega}{\partial x_j}, \tag{4}$$

in which k is

$$k = \tfrac{1}{2}\overline{u_i' u_i'}, \tag{5}$$

and ω is

$$\omega = \frac{\varepsilon}{k\beta^*}, \tag{6}$$

in which ε is the dissipation of turbulent kinetic energy

$$\varepsilon = \nu \overline{\frac{\partial u_i'}{\partial x_k}\frac{\partial u_i'}{\partial x_k}}. \tag{7}$$

In the preceding equations, τ_{ij} are the Reynolds stresses,

$$\tau_{ij} = \mu_T\left(\frac{\partial U_i}{\partial x_j} + \frac{\partial U_j}{\partial x_i}\right) - \tfrac{2}{3}\rho k \delta_{ij}, \tag{8}$$

u_i' is the fluctuating components of the velocity, δ_{ij} is the Kronecker delta ($\delta_{ij} = 1$ for $i = j$ and $\delta_{ij} = 0$ for $i \neq j$), ν_T is kinematic eddy viscosity, $\nu_T = \mu_T/\rho$, and β^* is one of the model closure constants.

σ_k in (3) and σ_ω, γ and β in (4) are given as

$$\sigma_k = F_1\sigma_{k1} + (1 - F_1)\sigma_{k2}, \tag{9}$$

$$\sigma_\omega = F_1\sigma_{\omega 1} + (1 - F_1)\sigma_{\omega 2}, \tag{10}$$

$$\gamma = F_1\gamma_1 + (1 - F_1)\gamma_2, \tag{11}$$

$$\beta = F_1\beta_1 + (1 - F_1)\beta_2, \tag{12}$$

in which σ_{k1}, σ_{k2}, $\sigma_{\omega 1}$, $\sigma_{\omega 2}$, γ_1, γ_2, β_1 and β_2, the model constants, are combined as a function of the distance z to the nearest wall with a so-called blending function, F_1.

The model constants for inner (wall) region are:

β_1	β^*	$\gamma_1 (= (\beta_1/\beta^*) - (\sigma_{\omega 1}\kappa^2/\sqrt{\beta^*}))$	σ_{k1}	$\sigma_{\omega 1}$
0.0750	0.09	0.567	0.85	0.5

and for the outer region:

β_2	β^*	$\gamma_2 (= (\beta_2/\beta^*) - (\sigma_{\omega 2}\kappa^2/\sqrt{\beta^*}))$	σ_{k2}	$\sigma_{\omega 2}$
0.0828	0.09	0.463	1.0	0.856

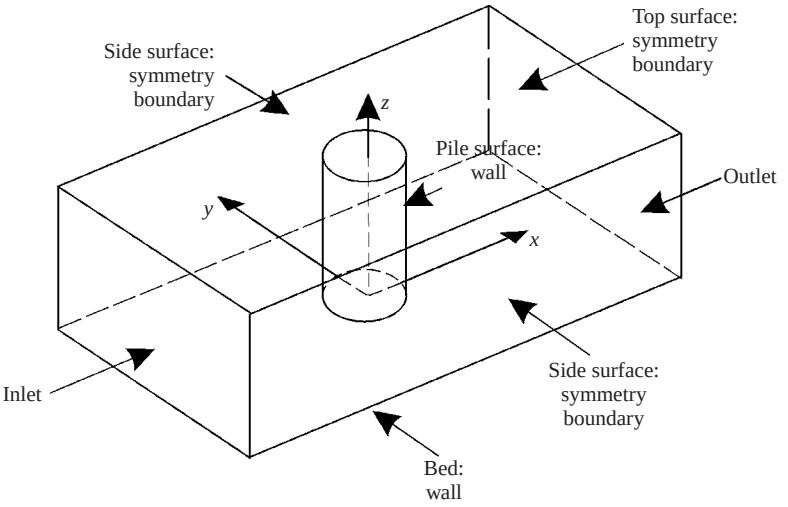

FIGURE 2. Boundaries.

in which $\kappa(=0.4)$ is the von Kármán constant.

The function F_1, on the other hand, is

$$F_1 = \tanh\left(\arg_1^4\right) \tag{13}$$

and

$$\arg_1 = \min\left[\max\left(\frac{\sqrt{k}}{0.09\omega z}; \frac{500\nu}{z^2\omega}\right); \frac{4\rho k\sigma_{\omega 2}}{(CD_{k\omega})z^2}\right] \tag{14}$$

with

$$(CD_{k\omega}) = \max\left(2\rho\frac{\sigma_{\omega 2}}{\omega}\frac{\partial k}{\partial x_j}\frac{\partial \omega}{\partial x_j}; 10^{-20}\right) \tag{15}$$

In the k–ω, SST model, the eddy viscosity is calculated from

$$\mu_T = \rho\frac{0.3k}{\max(0.3\omega; \Omega F_2)} \tag{16}$$

where Ω is the absolute value of the vorticity. The function F_2 in (16) is another blending function, defined by

$$F_2 = \tanh\left(\arg_2^2\right), \tag{17}$$

in which

$$\arg_2 = \max\left(2\frac{\sqrt{k}}{0.09\omega z}; \frac{500\nu}{z^2\omega}\right). \tag{18}$$

Both F_1 and F_2 take the value unity at the wall and gradually decrease and approach zero as the distance from the wall is increased.

2.3. *Boundary conditions*

The boundaries of the computational domain (figure 2) are inlet, outlet, symmetry boundaries and walls.

2.3.1. *Inlet and outlet boundary conditions*

(i) At the inlet, zero transverse, v, and vertical, w, velocities were specified. The inlet profiles for u, k and ω were based on the equilibrium profiles obtained from uniform-channel flow calculations with similar flow settings.

(ii) At the outlet, zero-gradient conditions ($\partial/\partial n = 0$), Neumann conditions, were applied for all quantities.

2.3.2. *Symmetry boundaries*

At the symmetry boundaries (i.e. at the sides and top surface of the computational domain, figure 2), Neumann conditions were applied for k and ω and for the three components of the velocity (u, v and w). As seen, the model does not have a free-surface facility; there is a 'lid' at the top surface. The implication of the latter is that the model cannot handle the situations where there is a significant amount of change in the free surface near the structure. This aspect of the flow is mainly controlled by the Froude number, Fr; the larger the value of Fr, the more pronounced the variation in the free-surface elevation. The is discussed in detail in § 5.1.

2.3.3. *Walls* (*the bed and the pile surface*)

(i) Zero velocity was specified for u , v and w.

(ii) Zero turbulent energy was specified for k when the wall was smooth, while the Neumann condition was applied when the wall was rough and transitional. Regarding the latter condition, experiments reveal that the Neumann condition is satisfied ($\partial k/\partial n = 0$) at the wall for rough boundaries, n being the direction normal to the wall (Nezu 1977; Sumer, Cokgor & Fredsøe 2001; Sumer *et al.* 2003). A validation exercise for the undisturbed-flow case revealed a much better agreement with the experiments (Nezu 1977; Sumer *et al.* 2001) when the boundary condition was taken in the form of the Neumann condition (Roulund 2000, p. 25).

(iii) The Dirichlet condition was applied for ω, namely,

$$\omega = S_r \frac{U_f^2}{\nu} \quad \text{at the wall,} \tag{19}$$

where $U_f = \sqrt{\tau_o/\rho}$ is the friction velocity based on the wall shear stress τ_o. The quantity S_r is a tuning parameter, and it is used to account for the bed roughness:

$$S_r = \begin{cases} \left(\dfrac{40}{k_s^+}\right)^3 & (k_s^+ < 20.2) \\ \dfrac{100}{(k_s^+)^{0.85}} & (k_s^+ > 20.2) \end{cases} \tag{20}$$

where $k_s^+ = (k_s U_f)/\nu$ is the wall roughness in wall units, and k_s is Nikuradse's equivalent sand roughness. Wilcox (1993) was the first to introduce the boundary condition in (19). The tuning parameter S_r was given by Wilcox (1993) as in (20), but with constants slightly different from those in (20) owing to the special implementation of the velocity boundary conditions. With the present constants (equation (20)), the friction velocity determined for a wide range of velocities for the case of the undisturbed flow was found to agree well with that obtained from the classic Colebrook and White equation (the diffference being less than 6 %, depending on the wall roughness, Roulund 2000, p. 23).

(iv) For the implementation of the preceding boundary condition, the wall shear stress, $\tau_0 (= \rho U_f^2)$, is required. In the present application, τ_0 was not calculated from

Calculation type	Rigid bed	Live-bed scour
Block dimension, N^3	32^3	16^3
Total number of cells	786×10^3	197×10^3
Number of cells across water depth	64	32
Number of cells around pile perimeter	128	64
Length of calculation domain	$20D$	$15D$
Width of calculation domain	$20D$	$18D$
Depth of calculation domain	$2D$	$2D$

TABLE 1. Characteristics of mesh in the numerical calculations.

$\tau_0 = (\mu + \mu_T)(\partial U_i/\partial x_j + \partial U_j/\partial x_i)_{Wall}$ as is traditionally done, but rather from the van Driest (1956) velocity profile

$$\frac{u}{U_f} = 2\int_0^{y^+} \frac{\mathrm{d}y^+}{1 + \sqrt{1 + 4\kappa^2 (y^+ + \Delta y^+)^2 \left[1 - \exp(-(y^+ + \Delta y^+)/A)\right]^2}}. \tag{21}$$

This improved the stability of the model and allowed a coarser mesh resolution at the bed. Here, $A(=25)$ is the van Driest damping factor, $y^+(= yU_f/\nu)$ is the distance from the wall in wall units, measured from the top of the roughness elements and Δy^+ is the coordinate shift (Rotta 1962; Cebeci & Chang 1978) given by

$$\Delta y^+ = 0.9\left[\sqrt{k_s^+} - k_s^+ \exp\left(-\frac{k_s^+}{6}\right)\right] \qquad (5 < k_s^+ < 2000), \tag{22}$$

in which k_s^+ is the roughness Reynolds number, $k_s^+ = k_s U_f/\nu$. In the implementation of (21), u is taken as the tangential velocity in the cell adjacent to the wall.

Similar implementation of the bed shear stress in the wall boundary conditions is reported in Sørensen (1995) for the k–ε model.

As a final remark in conjunction with §§2.2 and 2.3, it may be emphasized that the turbulence model incorporated in the present code is a well-tested model and has been used successfully in various contexts in computational fluid dynamics (Menter 1993; Wilcox 1993). The only changes made in the present implementation are the values of the constants in (20) which are slightly different from those originally given by Wilcox (1993) (item (iii) above), and the way in which the wall shear stress is calculated through the van Driest equation (item (iv) above).

2.4. *Computational mesh*

The momentum, continuity and turbulence-model equations are transformed into curvilinear coordinates, linearized and decoupled.

The computational mesh is based on a multi-block structure with each block containing N^3 computational cells where N is the number of cells in each spatial direction.

Two different types of calculation have been performed: (i) rigid-bed calculations; (ii) live-bed scour calculations;

Table 1 summarizes the mesh characteristics for the different types of calculation. It may be noted that $N = 32$ required prohibitively large computational times for the scour and unsteady-flow simulations.

Figure 3(*a*) shows a detailed picture of the mesh used for the rigid-bed calculations. During the live-bed scour calculations, the mesh is continuously updated to adjust the changes of the bed topography. Figure 3(*b*) illustrates an example of the mesh during the scour calculations.

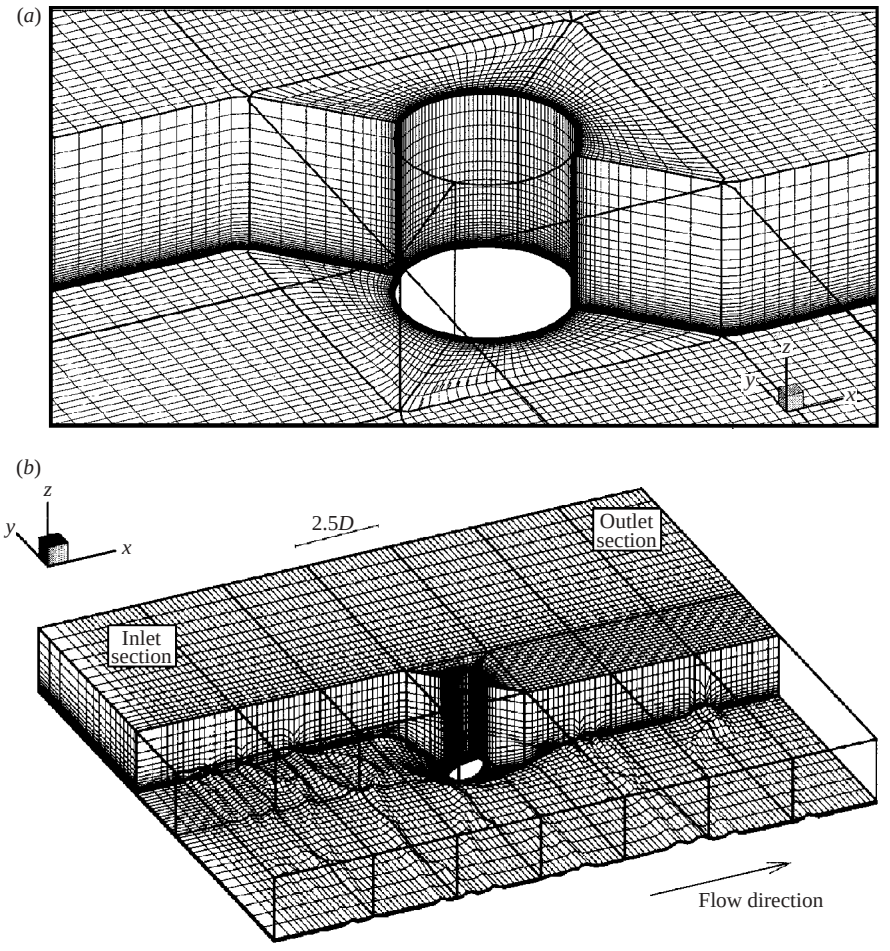

FIGURE 3. (*a*) Detail of mesh for rigid bed calculation. (*b*) Example of mesh for scour calculation.

3. Morphologic model

The morphologic model couples the flow solution with a sediment transport description, and routines for updating the computational mesh based on the mass balance of sediment.

There are three elements in the morphologic model: (i) the bedload; (ii) the sand slides, and (iii) the equation of continuity (mass balance) for sediment.

3.1. *Bedload*

A two-dimensional bedload description has been developed. This description is an extension of the bedload equation of Engelund & Fredsøe (1976) to a two-dimensional vectorial representation.

The bedload occurs on a slope (figure 4). $\boldsymbol{U}_b$ is the mean transport velocity of a particle moving as bedload. The fluid velocity at the particle position is $\boldsymbol{U}$, different from $\boldsymbol{U}_b$ (figure 4). Following Engelund & Fredsøe (1976), the latter velocity may be taken as $\boldsymbol{U} = a\boldsymbol{U}_f$ in which $\boldsymbol{U}_f$ is the friction velocity, and a is an empirical constant, taken as $a = 10$. (It may be noted that the constant a in Engelund & Fredsøe's study was determined by comparing the velocity of bedload particles expressed by

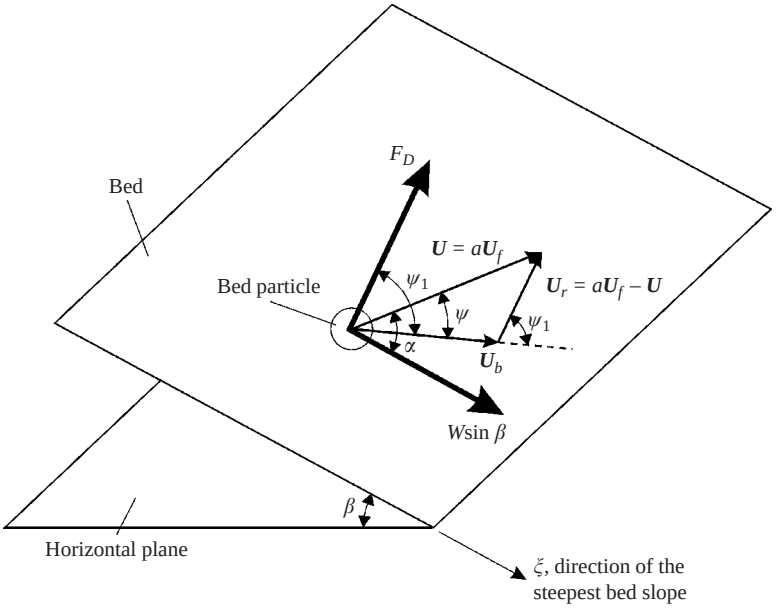

FIGURE 4. Force balance on a single moving particle on a sloping bed.

$U_b/U_f = a(1 - 0.7\sqrt{\theta_c/\theta})$ with the experimental data from studies of Luque (1974) and Meland & Norman (1966) (see figure 1 in Engelund & Fredsøe 1976). Here, θ is the Shields parameter and θ_c the critical value of the Shields parameter corresponding to initiation of motion at the bed, see (26) below).

The rate of bedload transport in volume per unit time and per unit width, $\boldsymbol{q}_b$, is related to $\boldsymbol{U}_b$ by the following equation (Engelund & Fredsøe 1976)

$$\boldsymbol{q}_b = \tfrac{1}{6}\pi d^3 \frac{p_{EF}}{d^2}\boldsymbol{U}_b \tag{23}$$

in which d is the grain size, and p_{EF} is the percentage of particles in motion in the surface layer of the bed. As seen from the above equation, the bedload transport is determined by two quantities: p_{EF} and $\boldsymbol{U}_b$. Each quantity is now considered individually.

3.1.1. *Percentage of particles in motion in the surface layer of the bed*

Engelund & Fredsøe (1976) give the following semi-empirical expression for p_{EF},

$$p_{EF} = \left[1 + \left(\frac{\tfrac{1}{6}\pi\mu_d}{\theta - \theta_c}\right)^4\right]^{-1/4}, \tag{24}$$

in which μ_d is the dynamic friction coefficient, taken as 0.51 (Fredsøe & Deigaard 1992, p. 218), θ is the Shields parameter associated with the skin friction and θ_c is the critical value of θ for the initiation of motion at the bed. The same expression has been used for the present calculations with the critical Shields parameter calculated by

$$\theta_c = \theta_{c0}\left(\cos\beta\sqrt{1 - \frac{\sin^2\alpha\tan^2\beta}{\mu_s^2}} - \frac{\cos\alpha\sin\beta}{\mu_s}\right), \tag{25}$$

in which θ_{c0} is the critical Shields parameter for a horizontal bed, taken as 0.05, μ_s is the static friction coefficient, taken as $\mu_s = 0.63$ for the sand used in the present simulation (Lambe & Whitman 1969, p. 149), and α is the angle between the flow velocity vector $\boldsymbol{U}$ and the direction of the steepest bed slope ξ (figure 4). It may be noted that changing θ_c with that given in (25) ensures that the 'slope effect' is accounted for. The Shields parameter in (24) is defined by

$$\theta = \frac{U_f^2}{(s-1)gd}, \tag{26}$$

in which $s = \rho_s/\rho$ is the specific gravity of the sediment grains, and g is the acceleration due to gravity. U_f in (26) is taken as the magnitude of the friction-velocity vector $\boldsymbol{U}_f$ associated with the skin friction.

(Dey 2003, derived an equation for the critical bed shear stress in the general case where the bed surface has a slope in two directions (i.e. longitudinal and transverse directions). In his derivation, Dey also considered a lift force on the particle. Dey's equation reduces to that given in (25) when the slope in the longitudinal direction is set equal to zero, and the lift force, F_L, is omitted. The latter is justified because the lift is small compared with the submerged weight of the particle, W, at the threshold of the motion, namely $F_L/(W\cos\beta) = O(0.1)$. The latter can be readily verified, using the lift force data existing in the literature, e.g. Einstein & El Samni 1949, and Sumer 1984).

3.1.2. *Mean transport velocity of particle*

First, we consider the forces on a bedload particle (figure 4). There are two kinds of force: The agitating forces and the stabilizing forces. The former forces are the agitating force due to gravity and that due to flow.

(i) The agitating force due to gravity in the direction of the steepest bed slope is

$$W\sin\beta, \tag{27}$$

in which

$$W = \tfrac{1}{6}\pi\rho g(s-1)d^3. \tag{28}$$

(ii) The agitating forces due to flow are the drag force and the lift force. Following Engelund & Fredsøe (1976, p. 297), this force may be written in the form of a drag force

$$F_D = \tfrac{1}{2}\rho c\frac{\pi}{4}d^2U_r^2, \tag{29}$$

in which c is the force coefficient, and U_r is the velocity of the flow (at the particle position) relative to the particle:

$$\boldsymbol{U}_r = \boldsymbol{U} - \boldsymbol{U}_b = a\boldsymbol{U}_f - \boldsymbol{U}_b. \tag{30}$$

The stabilizing force, on the other hand, is

$$(W\cos\beta)\mu_d, \tag{31}$$

which is in the direction opposite to the particle motion. Here, μ_d is the dynamic friction coefficient.

It can readily be shown that the force coefficient c in (29) is actually $c = C_D + \mu_d C_L$, the coefficients C_D and C_L being the drag and the lift coefficients. c can be found from the force balance for a bedload particle at the critical velocity on a horizontal

bed:

$$c = \frac{4\mu_s}{3a^2\theta_{c0}}. \tag{32}$$

However, Luque (1974) found from his experiments (see also Engelund & Fredsøe 1976, p. 298, and Fredsøe & Deigaard 1992; p. 211):

$$c = \frac{4\mu_s}{3a^2\left(\frac{1}{2}\theta_{c0}\right)}. \tag{33}$$

The latter equation has been used in the present calculations.

Next, we consider the two components of the equation of the particle motion (figure 4).

The equation of motion in the direction of the particle motion, considering that the particle is, on average, moving with a constant velocity:

$$F_D \cos\Psi_1 + W \sin\beta \cos(\alpha - \Psi) - (W \cos\beta)\mu_d = 0. \tag{34}$$

The equation of motion in the direction perpendicular to $\boldsymbol{U}_b$, on the other hand, reads:

$$F_D \sin\Psi_1 - W \sin\beta \sin(\alpha - \Psi) = 0 \tag{35}$$

There are also the following geometric relations from figure 4

$$U_r \sin\Psi_1 - aU_f \sin\Psi = 0, \tag{36}$$

and

$$U_r \cos\Psi_1 - aU_f \cos\Psi + U_b = 0. \tag{37}$$

Equations (34)–(37) are to be solved for the four unknowns, namely U_b, U_r, Ψ and Ψ_1. Once U_b and Ψ are determined (and therefore $\boldsymbol{U}_b$ is obtained), then inserting $\boldsymbol{U}_b$ and p_{EF} (from (24) and (25)) in (23) will give the bedload transport $\boldsymbol{q}_b$. These equations have been solved in their full forms with the Newton–Raphson technique.

3.2. *Sand slide*

Observations show that, during the development of scour holes, there are areas at the upstream face of the scour hole where the local bed slope exceeds the angle of repose, and, as a result, shear failures occur at these locations. Two 'ingredients' of this latter process are that, first of all, the backward flow at the base of the pile erodes the foot of the upstream slope of the scour hole (A in figure 5), and secondly, there is a continuous sediment supply into the scour hole from upstream (B in figure 5). The video frame, for example, at $t = 5$ min (figure 30*c*) reveals these processes.

Our visual observations have indicated that, in the main upstream part of the scour hole, the bed collapses when the bed slope β exceeds approximately the angle of repose, $\beta_r \simeq 32^\circ$, by a few degrees. They have also showed that the shear failure in the soil occurs just below the bed surface, and sand slides down towards the centre of the scour hole. After each sand slide, the bed slope is a few degrees lower than the angle of repose. It may be noted that the 'oversteepening' of slope before sand slide is known to occur in geological/sedimentological/bedform processes (see, e.g. Allen 1985, pp. 68–69).

Based on these observations, a 'sand slide' procedure was developed to calculate the new slope of the bed:

(i) Calculate a new sediment transport rate when the local bed slope exceeds $\beta_r + 2^\circ$.

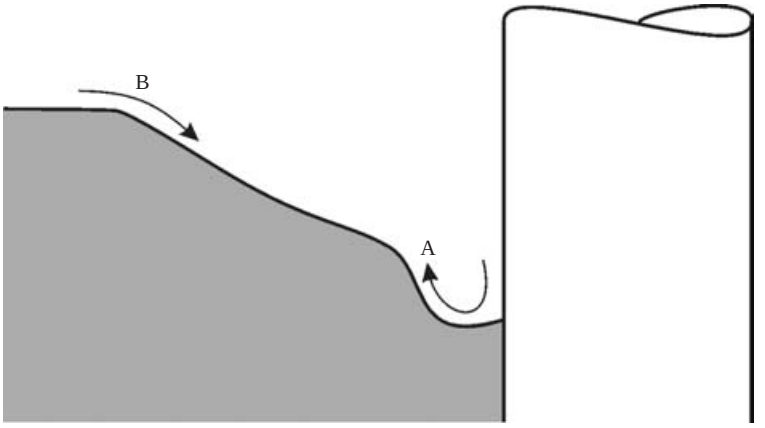

FIGURE 5. Two major effects, A and B, to cause sand slide. A, erosion of the foot of the upstream slope; B, continuous supply of sediment.

(ii) Do this, based on a new particle velocity U_b, obtained from the following equation:

$$W \sin\beta - \mu_d W \cos\beta - \tfrac{1}{2}\rho C_D \frac{\pi}{4} d^2 U_b^2 = 0. \tag{38}$$

(This is basically the equation of motion for a sediment particle (undergoing the sand slide) in the direction of the particle motion, considering that the particle is, on average, moving with a constant velocity in a still water).

(iii) Update the bed with the morphology scheme (described in the following section) used for the ordinary bedload.

(iv) Repeat this procedure until the local bed slope is reduced to $\beta_r - 2^\circ$.

In this procedure, a pseudo time step was used since it was assumed that the sand slide takes place instantaneously. It may be noted that the work of Olsen & Kjellesvig (1998) also takes account of the sand slide in the development of the scour hole.

3.3. *Morphologic scheme*

The mass balance for sediment at each grid point on the bed is

$$\frac{\partial h}{\partial t} = \frac{-1}{1-n} \frac{1}{A} \sum_{i=1}^{4} [(\boldsymbol{q}_{b,i} \cdot \boldsymbol{n}_i)|l_i|], \tag{39}$$

in which h is the bed elevation, n is the porosity (taken as $n = 0.4$ in the present calculations), A is the projected area (on the (x, y)-plane) of a small bed-surface element, i indicates the number assigned to each side of the projected area ($i = 1, \ldots, 4$), $\boldsymbol{n}_i$ is the normal vector at the ith side of the projected area, $\boldsymbol{q}_{b,i}$ is the sediment-transport vector at the ith side of the projected area and $|l_i|$ is the length of the ith side of the bed element.

The procedure in the computations was as follows: (i) generate the mesh; (ii) calculate the flow; (iii) calculate the sediment transport due to bed load; (iv) update the bed; (v) check the sand slide; and (vi) return to Step 1. The morphologic time step in the calculations was 0.02 s initially, and gradually raised to 0.1 s. The computational time for a single test (where the scour starts with an initially plane bed and continues until the scour process attains its equilibrium state) was 2.5 months on an Alpha 21264 workstation, equivalent to a 1500 MHz Pentium IV.

Finally, it may be noted that, in the present model, the sediment transport is taken as bedload (no suspended-load sediment transport is considered). To our knowledge, no study is yet available, investigating the effect of the suspended load on scour. However, the data reported in Baker (1986) (where the scour regimes are covered in a systematic manner from the clear-water scour to the live-bed scour (i) with bed-load, (ii) with bed-load and suspended load, and (iii) with suspended-load sheet-flow) suggests that this effect is not radically significant in terms of the equilibrium scour depth (see Melville & Sutherland 2000, p. 493; Sumer & Fredsøe 2002, p. 179). However, the suspension process can increase the time rate of scour in the initial stages (see § 6.2).

4. Experiments

4.1. *Rigid-bed experiments*

The rigid-bed experiments were conducted with a vertical circular pile in a steady current. The purpose of these experiments was to obtain data to validate the hydrodynamic model.

The pile diameter was $D = 53.6$ cm. The surface of the pile was hydraulically smooth. The pile base was sealed along its perimeter at the bottom.

Two kinds of experiments were made: (i) the smooth-bed experiments (Test 1); and (ii) the rough-bed experiments (Test 2) where the bottom of the flume was covered with a single layer of crushed stones; the roughness height of the stones was $k = 7$ mm. The former experiments were conducted in a flume, 35 m long and 3 m wide, while the latter experiments were conducted in another flume, 28 m long and 4 m wide. In both experiments, the water depth was maintained at 54 cm and the approach velocity at $V = 32.6\,\mathrm{cm\,s^{-1}}$. The velocity V was obtained from integration of the velocity profile. Regarding the blockage effect, the potential flow theory (see e.g. Sumer & Fredsøe 1997, p. 126) gives an increase in the flow velocity of only 3 % at the sidewalls in the case of the 3 m wide flume and less than 2 % in the case of the 4 m wide flume, and therefore the blockage effect did not pose any significant problem.

Two kinds of measurements were made: (i) velocity measurements; and (ii) bed shear stress measurements.

The velocity measurements were made in the plane of symmetry upstream and downstream of the pile. A two-component DANTEC 'pen-size' laser-Doppler anemometer (LDA) was used in the measurements. The LDA system comprised a two-colour high-performance fibre optic system with a DANTEC 60×17 14 mm fibre optic probe head and a 300 mW argon-ion laser, used in backscatter mode with two DANTEC 55N11 frequency shifters and two 57N10 Burst Spectrum Analyzers (BSA) in the smooth-bed experiments. The 300 mW laser was replaced with a 6 W argon laser in the rough-bed experiments where two DANTEC 55N21 frequency trackers were used instead of the BSAs, as these instruments were available at the time of these experiments. The focal length of the pen-size probe (with a specially built adapter) was 8 cm. The dimensions of the measurement volume ($d_x \times d_y \times d_z$) were $1.5\,\mathrm{mm} \times 0.12\,\mathrm{mm} \times 0.12\,\mathrm{mm}$.

The bed shear stress was measured with a DANTEC one-component 55R46 hot-film probe. These measurements were conducted only with the smooth bed. (The working principle of the hot-film technique breaks down for rough walls, and therefore this technique cannot be applied to such cases, Hanratty & Campbell 1983). The probe was mounted flush to the bed. It was calibrated in position, using a small three-sided calibration channel of 1 mm in depth and 30 mm in width, placed over the probe.

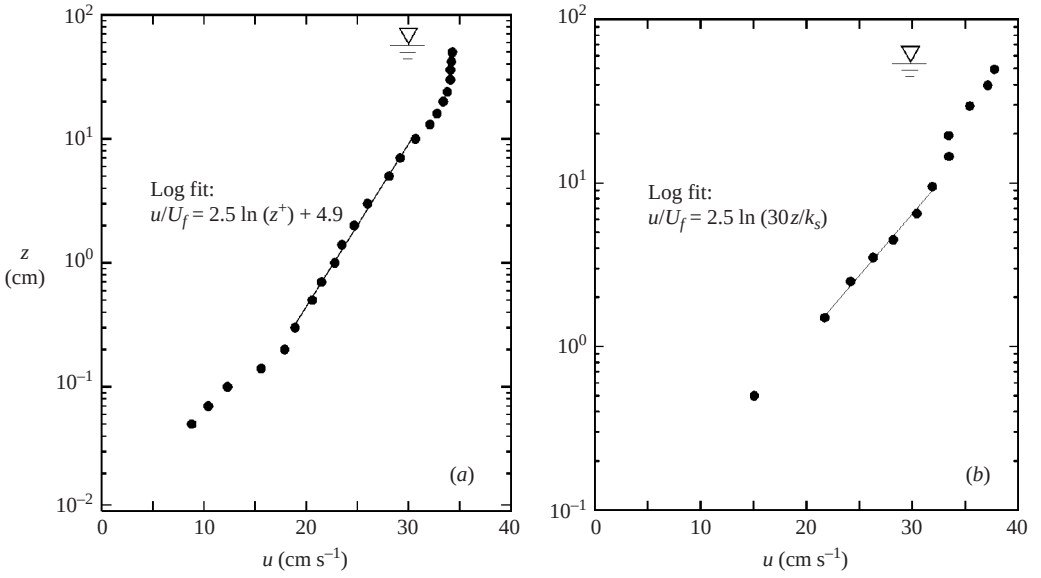

FIGURE 6. Undisturbed velocity profile at the measurement section for the rigid bed experiments. (*a*) Test 1, smooth bed, $U_f = 1.3\,\mathrm{cm\,s^{-1}}$. (*b*) Test 2, rough bed, $U_f = 2.3\ \mathrm{cm\,s^{-1}}$, $k_s = 1.0\,\mathrm{cm}$. z is measured from theoretical bed.

Further information about the probe and the calibration procedure can be found in Sumer *et al.* (1993).

In both the smooth-bed case and the rough-bed case, the pile was placed 20 m downstream of the inlet section.

Figures 6(*a*) and 6(*b*) show the measured, undisturbed mean velocity profiles at the measurement sections in the two experiments, respectively. In the figure, U_f is the friction velocity,

$$U_f = \sqrt{\frac{\tau_\infty}{\rho}}, \tag{40}$$

and z^+ is the normalized distance from the bed,

$$z^+ = \frac{zU_f}{\nu}, \tag{41}$$

Here, τ_∞ is the undisturbed bed shear stress, ρ the fluid density and ν the kinematic viscosity.

Table 2 summarizes the test conditions in the rigid-bed experiments. In the table, $Re_{\delta,V}$ is the boundary-layer thickness Reynolds number,

$$Re_{\delta,V} = \frac{V\delta}{\nu}, \tag{42}$$

$Re_{D,V}$ the pile Reynolds number,

$$Re_{D,V} = \frac{VD}{\nu}, \tag{43}$$

Note that the Reynolds numbers are based on the mean flow velocity V. Also, in the table, Fr is the Froude number defined by

$$Fr = \frac{V}{\sqrt{gh}}, \tag{44}$$

Test	(1)	1	2
Bed	(2)	Rigid	Rigid
Smooth bed/rough bed	(3)	Smooth	Rough
Water depth h (cm)	(4)	54	54
Boundary layer thickness δ (cm)	(5)	54	54
Mean flow velocity V (cm s^{-1})	(6)	32.6	32.6
Pile diameter D (cm)	(7)	53.6	53.6
$Re_{\delta,V} = V\delta/\nu$	(8)	1.8×10^5	1.8×10^5
$Re_{D,V} = VD/\nu$	(9)	1.7×10^5	1.7×10^5
$Fr = V/(gh)^{1/2}$	(10)	0.14	0.14
Bed roughness height k (cm)	(11)	–	0.7
Friction velocity U_f (cm s^{-1})			
From Log. Fit	(12)	1.3	2.3
From Hot-film Meas.	(13)	1.5	–
Bed Nikuradse equivalent sand Roughness k_s (cm)	(14)	–	1.0
$k_s^+ = k_s U_f/\nu$	(15)	–	230

TABLE 2. Test conditions for the rigid-bed experiments.

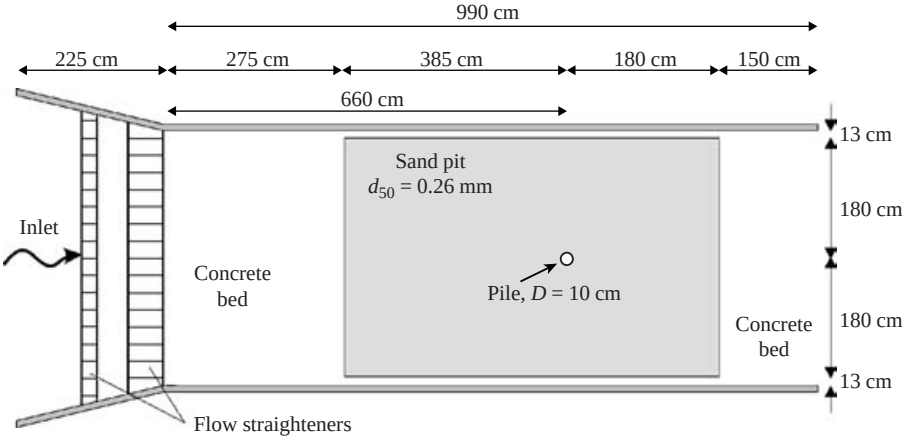

FIGURE 7. Test set-up for the scour experiment.

in which h is the flow depth. Moreover, in table 2, k_s^+ is the roughness Reynolds number corresponding to Nikuradse's equivalent sand roughness of the bed:

$$k_s^+ = \frac{k_s U_f}{\nu}, \tag{45}$$

4.2. *Scour experiment*

The purpose of the scour experiment was, first of all, to obtain a detailed description of the scour process so that the present morphologic model could be set up accordingly, and secondly, to obtain data, which together with the existing data, help to verify the model. The scour experiment (Test 3) was conducted in a current flume with a sand pit (figure 7). The water depth was 40 cm, and the undisturbed mean flow velocity $V = 46$ cm s^{-1}. The model pile, a 10 cm diameter circular cylinder with a hydraulically smooth surface, was placed in the sediment bed extending down to the bottom of the sand pit. The pile Reynolds number was $Re_{D,V} = 4.6 \times 10^4$. The sand size was $d_{50} = 0.26$ mm with a geometric standard deviation (the sediment gradation)

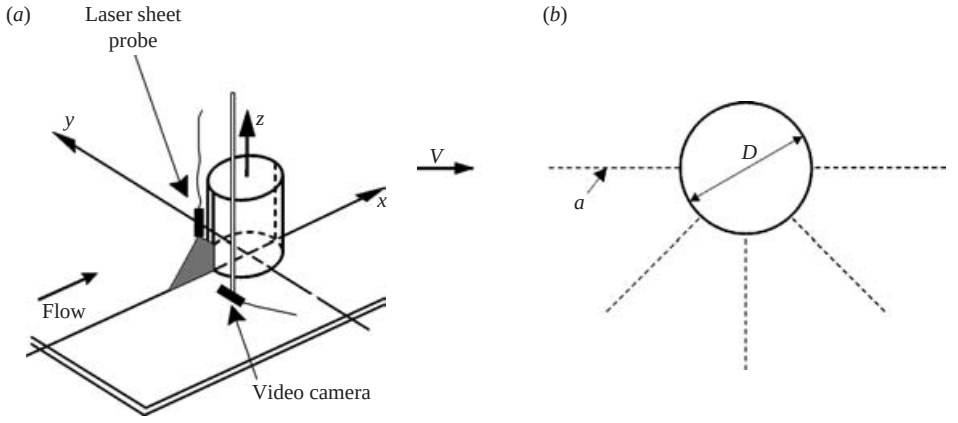

FIGURE 8. (*a*) Flow and scour visualization set-up for Test 3. (*b*) Radial planes videotaped in the flow/scour experiment.

of $\sigma_g = d_{85}/d_{50}$ (or $\sqrt{d_{84}/d_{16}}$, see Raudkivi 1998, p. 10) = 1.5 in which d_{85}, d_{50} and d_{15} correspond to the grain size of which, respectively, 85 %, 50 % and 15 % are finer. The ratio between the approach velocity and the critical velocity for the initiation of sediment motion was $V/V_{cr} = 1.25$ in which $V_{cr} = 37.5\,\mathrm{cm\,s^{-1}}$, corresponding to $\theta_{cr} = 0.05$, the critical value of the Shields parameter estimated from the Shields diagram for the initiation of motion at the bed (see, e.g. Sumer & Fredsøe 2002, p. 10 for the Shields diagram). The flow and scour processes around the pile were visualized, using a DANTEC 2.5 mm thick vertical sheet of laser light as a light source (figure 8*a*). The flow was made visible with fluorescent dye as well as with sediment grains. A miniature underwater video camera (figure 8*a*) was used to videotape the flow/scour processes. This exercise was repeated at five radial (vertical) sections sketched in figure 8(*b*) to obtain a complete picture of these processes around the pile.

The scour was in the live-bed regime. This was revealed by the presence of bed ripples outside the scour hole, as will be seen later (figure 32). The ripples were of a three-dimensional nature, 3–4 cm high and 10–15 cm long.

Apart from the flow-visualization experiments described above, the time development of scour depth at both the upstream side and the downstream side of the pile was monitored. No sediment feeding at the inlet of the sand pit was implemented in the experiments. This was because the bed lowering reached the test section about 4 h after the test started, a time period significantly larger than the time scale of scour (i.e. ~2 h at the upstream side and ~3 h at the downstream side of the pile, as will be detailed later).

Velocities in the scour experiment (in the undisturbed case) were measured with a micro propeller. Figure 9 displays the undisturbed mean velocity profile at the test section (figure 7). The distance from the bed, z, in the figure is measured from the mean bed level. Given the uncertainty imposed by the ripple-covered live bed, no refinement with regard to the precise location of the theoretical bed was sought. Figure 9 indicates that the velocity profile can be approximated by the logarithmic law,

$$\frac{u}{U_f} = 2.5 \ln\left(30\frac{z}{k_s}\right) \tag{46}$$

within the lower half of the flow depth. The figure also indicates that the boundary-layer thickness can be taken as $\delta = 20\,\mathrm{cm}$. Note that, owing to the relatively short

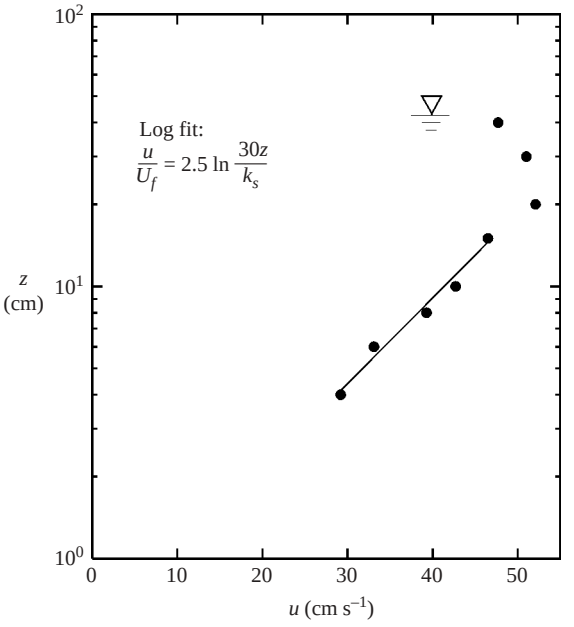

FIGURE 9. Undisturbed mean velocity profile in Test 3. z is measured from the mean level of ripples.

Test	(1)	3
Bed	(2)	Loose sand
Water depth h (cm)	(3)	40
Boundary-layer thickness δ (cm)	(4)	20
Mean flow velocity V (cm s^{-1})	(5)	46
Pile diameter D (cm)	(6)	10
$Re_{\delta,V} = V\delta/\nu$	(7)	9.2×10^4
$Re_{D,V} = VD/\nu$	(8)	4.6×10^4
$Fr = V/(gh)^{1/2}$	(9)	0.23
Grain size d_{50} (mm)	(10)	0.26
Gradation σ_g	(11)	1.5
Friction velocity U_f (cm s^{-1})	(12)	4.8
Friction velocity due to skin friction U'_f (cm s^{-1})	(13)	2.8
Shields Parameter θ	(14)	0.55
Shields parameter corresponding to U'_f θ'	(15)	0.19
Nikuradse equivalent sand roughness k_s (cm)	(16)	15
$k'_s = 2.5\, d_{50}$ (mm)	(17)	0.55
$k'^{+}_s = k'_s U'_f/\nu$	(18)	17

TABLE 3. Test conditions for the scour experiment.

distance from the inlet (660 cm, see figure 7), the boundary layer was not developed across the entire depth at the test section. The quantity k_s in (46) is Nikuradse's equivalent sand roughness corresponding to the ripple-covered bed, and the logarithmic fit gives $k_s = 15$ cm. The friction velocity from the logarithmic fit (equation (46)), on the other hand, is found to be $U_f = 4.8$ cm s^{-1} while the skin friction part of the latter friction velocity is estimated to be $U'_f = 2.8$ cm s^{-1}, using Engelund's (1966) relation.

The experimental conditions in the scour test (Test 3) are summarized in table 3.

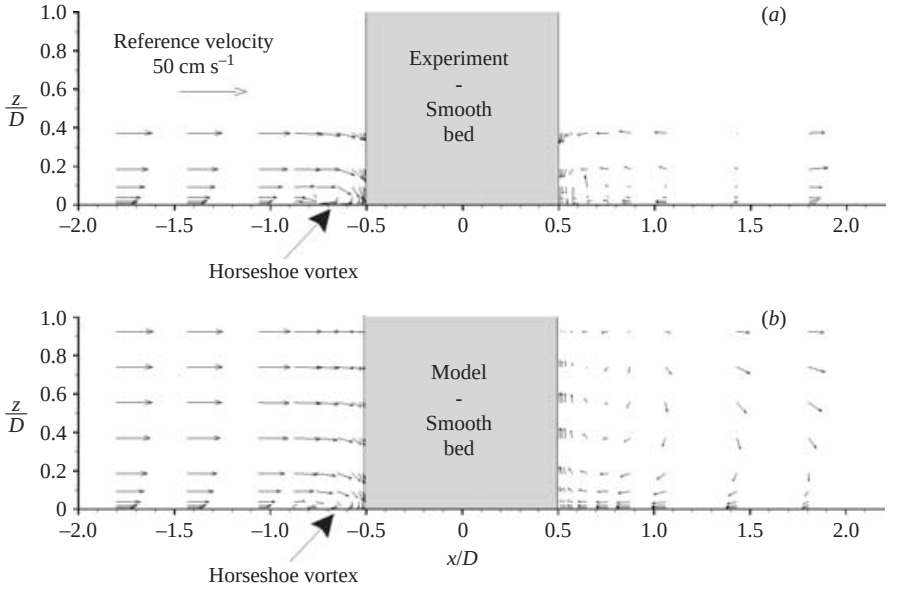

FIGURE 10. Velocity field in the plane of symmetry. Smooth rigid bed (Test 1).

5. Rigid-bed flow simulations

5.1. *Validation of the model*

The model has been validated against (i) the present experiments and (ii) the experiments of others. Three kinds of quantities are compared with their counterparts in the experiments: (i) the velocity; (ii) the pressure; and (iii) the bed shear stress.

Figure 10 shows the measured velocity field in the plane of symmetry from Test 1, the smooth bed case (table 2), of the present experiments, compared with that obtained from the steady-state solution of the numerical model. Figures 11 and 12, on the other hand, show the measured and calculated horizontal, u, and vertical, w, velocities for various values of the distance, z, from the bed for the same test (Test 1).

Figures 13–15 compare the corresponding results for the rough-bed case (Test 2, table 2).

Figures 11–12 and 14–15 show that, at the upstream side of the pile, there is good agreement between the numerical simulations and the measurements, although the velocities for small values of z very near the pile seem to be somewhat underpredicted in the numerical simulations. Furthermore, the comparisons in figures 10 and 13 indicate that the horseshoe vortex (figure 1) is predicted well by the numerical model. It may be noted that the curvature in the circulation pattern in the experimental results (figure 10a) is stronger on the upstream side than in the model in the range $-0.7 \lesssim x/D \lesssim -0.5$ below $z/D = 0.2$. This is due to the underpredicted vertical velocities in the model (figure 12, $z = 0.5$; 1.0; and 2.0 cm).

As for the downstream side of the pile (in the plane of symmetry), figure 10(a) indicates that a mean anticlockwise circulation is present in the experiments in Test 1, the smooth-bed case. By introducing the rough-bed conditions (Test 2), however, the mean circulation behind the pile changes its direction; namely, a clockwise circulation forms behind the pile, as revealed by figure 13(a).

Now, the numerical model was not able to capture the aforementioned anticlockwise circulation observed in the smooth-bed experiment (see the lee side of the pile in

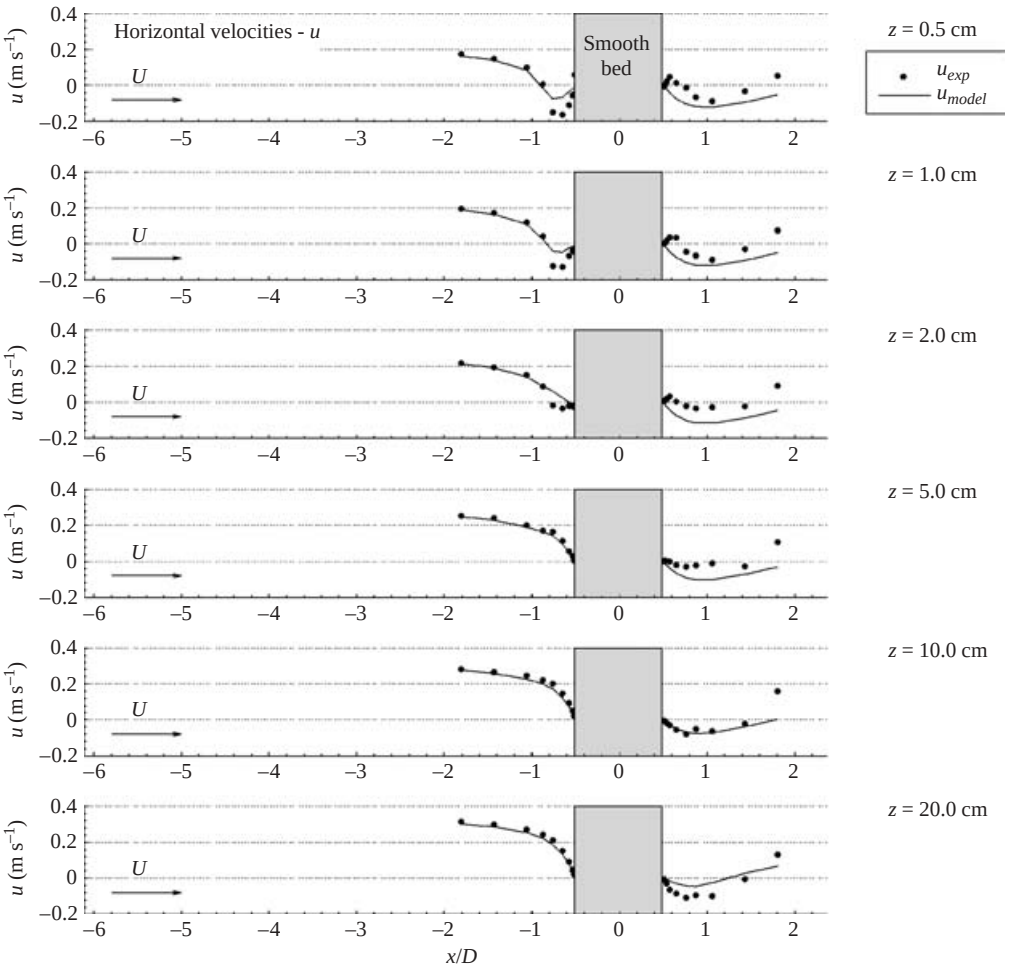

FIGURE 11. Horizontal velocity, u ($\mathrm{m\,s^{-1}}$), in the plane of symmetry at different distances from the bed. Smooth rigid bed (Test 1).

figure 10(*b*), and also see the w velocities at the lee side of the pile at distances $z = 2 - 20\,\mathrm{cm}$ in figure 12) while it did capture the clockwise circulation in the rough-bed experiment (cf. figure 13). No clear explanation has been found for this behaviour.

Figure 16 compares the bed shear stress along the x-axis calculated from the model with that measured in the experiments in Test 1 (table 2). The negative bed shear stress corresponds to the location of the horseshoe vortex in front of the pile (figure 1). The figure shows that the numerical and experimental results agree very well outside the horseshoe vortex. The agreement of the model with the trend in the data is also good inside the horseshoe vortex for $x/D < -0.75$. However, for $-0.75 < x/D < -0.5$, the bed shear stress is apparently underpredicted by the numerical model, the maximum difference between the model and the experiment being more than 30 %. The latter is consistent with the picture obtained in conjunction with the velocity measurements at the upstream side of the pile at $z = 0.5 - 2\,\mathrm{cm}$ presented in figure 11. No clear explanation has been found for the observed discrepancy between the numerical model and the experiments.

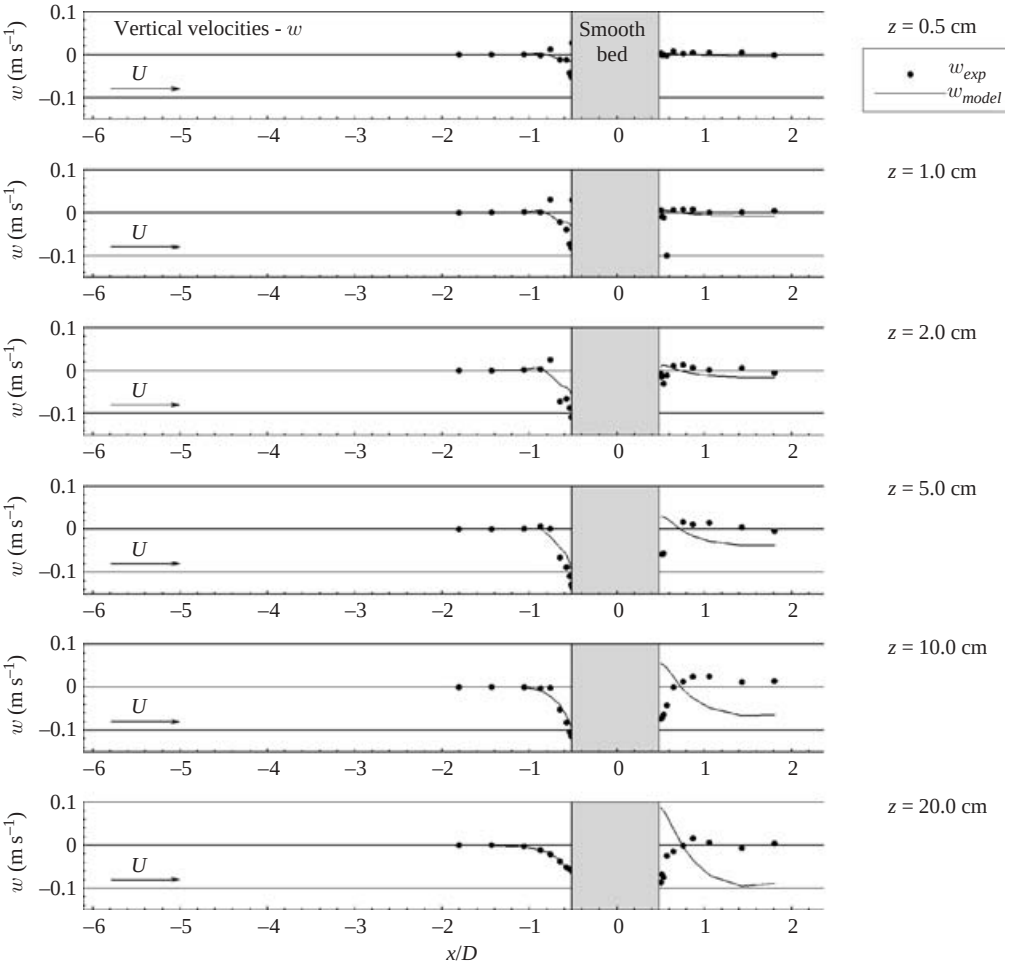

FIGURE 12. Vertical velocity, w ($\mathrm{m\,s^{-1}}$), in the plane of symmetry at different distances from the bed. Smooth rigid bed (Test 1).

Figure 17 compares the amplification of the bed shear stress obtained from the present model and that from Hjorth's (1975) smooth-bed experiments. Here the amplification of the bed shear stress is defined by

$$\alpha_\tau = \frac{|\tau_0|}{\tau_\infty}, \tag{47}$$

in which τ_0 is the bed shear stress and τ_∞ is the undisturbed bed shear stress. The bed is smooth. $h = \delta = 20\,\mathrm{cm}$, $V = 30\ \mathrm{cm\,s^{-1}}$, $D = 5\,\mathrm{cm}$, $Re_{\delta,V} = 6 \times 10^4$, $Re_{D,V} = 1.5 \times 10^4$ and $\delta/D = 4$. The agreement between the present calculations and the measurements is reasonable; the maximum value of the bed shear stress and also the location of the maximum bed shear stress are captured well.

Graf & Yulistiyanto (1998) also measured the bed shear stress. The latter was obtained from the Reynolds stress profiles. They report that the Reynolds stress measurements near the bed are doubtful because of the limitations of their measuring technique. Nevertheless, they argue that the only apparent conclusive evidence from their measurements is that the bed shear stress reaches its largest values in the plane

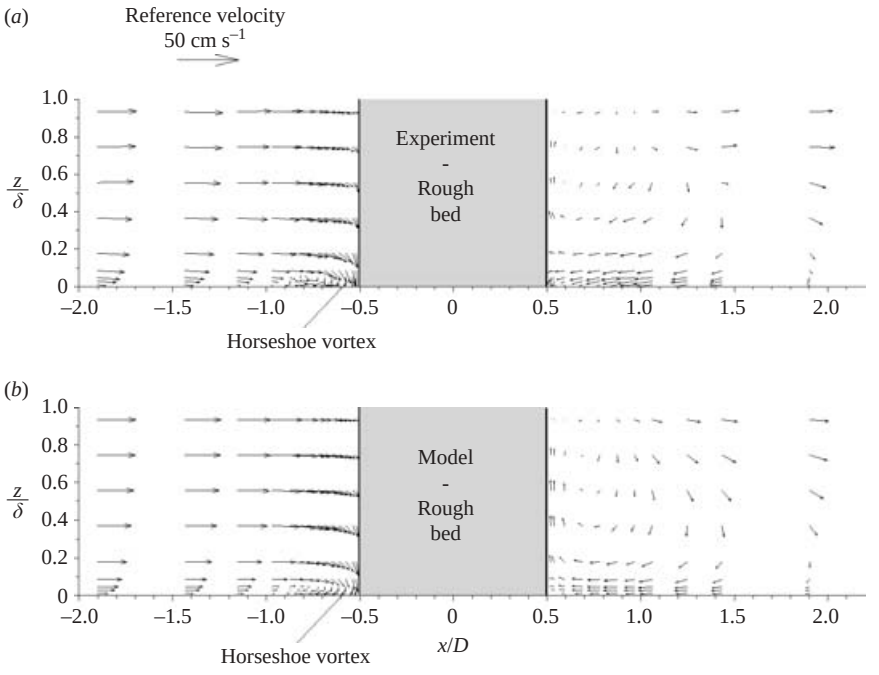

FIGURE 13. Velocity field in the plane of symmetry. Rough rigid bed (Test 2).

at 45° (this is for both tests they carried out). This result is in good agreement with the present numerical result in figure 17(*a*).

Figures 18(*a*) and 18(*b*) compare the present simulation results with the pressure measurements of Dargahi (1989). The bed is smooth. The test conditions are: $h = \delta = 20\,\text{cm}$, $V = 26\,\text{cm s}^{-1}$, U (the free-stream velocity) $= 30\,\text{cm s}^{-1}$, $D = 15\,\text{cm}$, $Re_{\delta,V} = 5.2 \times 10^4$ and $Re_{D,V} = 3.9 \times 10^4$. Figure 18(*a*) depicts the stagnation pressure across the depth at the upstream edge of the pile, while figure 18(*b*) depicts the pressure at the bed along the upstream line of symmetry. The quantity plotted, C_p, is the pressure coefficient. The agreement between the model simulation and the measurement is good. It may be noted that Dargahi (1989) relates the narrow plateau in the pressure at the bed (in the interval $-0.9 < x/D < -0.7$, figure 18*b*) to the presence of the horseshoe vortex. Although shifted to slightly higher $|x/D|$ values, this plateau is also captured in the present numerical simulation.

One of the referees called for a comparison between the present numerical model and Graf & Yulistiyanto's (1998) experiments where the velocity was measured in radial planes at various angles. This exercise was carried out and the results are plotted in figure 19. The test conditions were as follows: the water depth was $h = 18.5\,\text{cm}$, the mean flow velocity $V = 67\,\text{cm s}^{-1}$, the pile diameter $D = 22\,\text{cm}$, and the bed was smooth. As seen from figure 19, although the model captures the main features of the flow at $\Theta = 0°$ and $\Theta = 45°$ reasonably well, this is not the case for the radial planes $\Theta = 90°$, $\Theta = 157.5°$ and $\Theta = 180°$. This discrepancy arises because the numerical model has a 'lid' at the top surface of the computational domain (a symmetry boundary, figure 2) rather than a free surface. In the experiment, however, the free surface exhibits a substantial amount of variation in the vicinity of the cylinder (figure 19 and see figure 20 for a schematic description). There is a runup in front of the cylinder and a 'depression' around the side edge and at the back of the

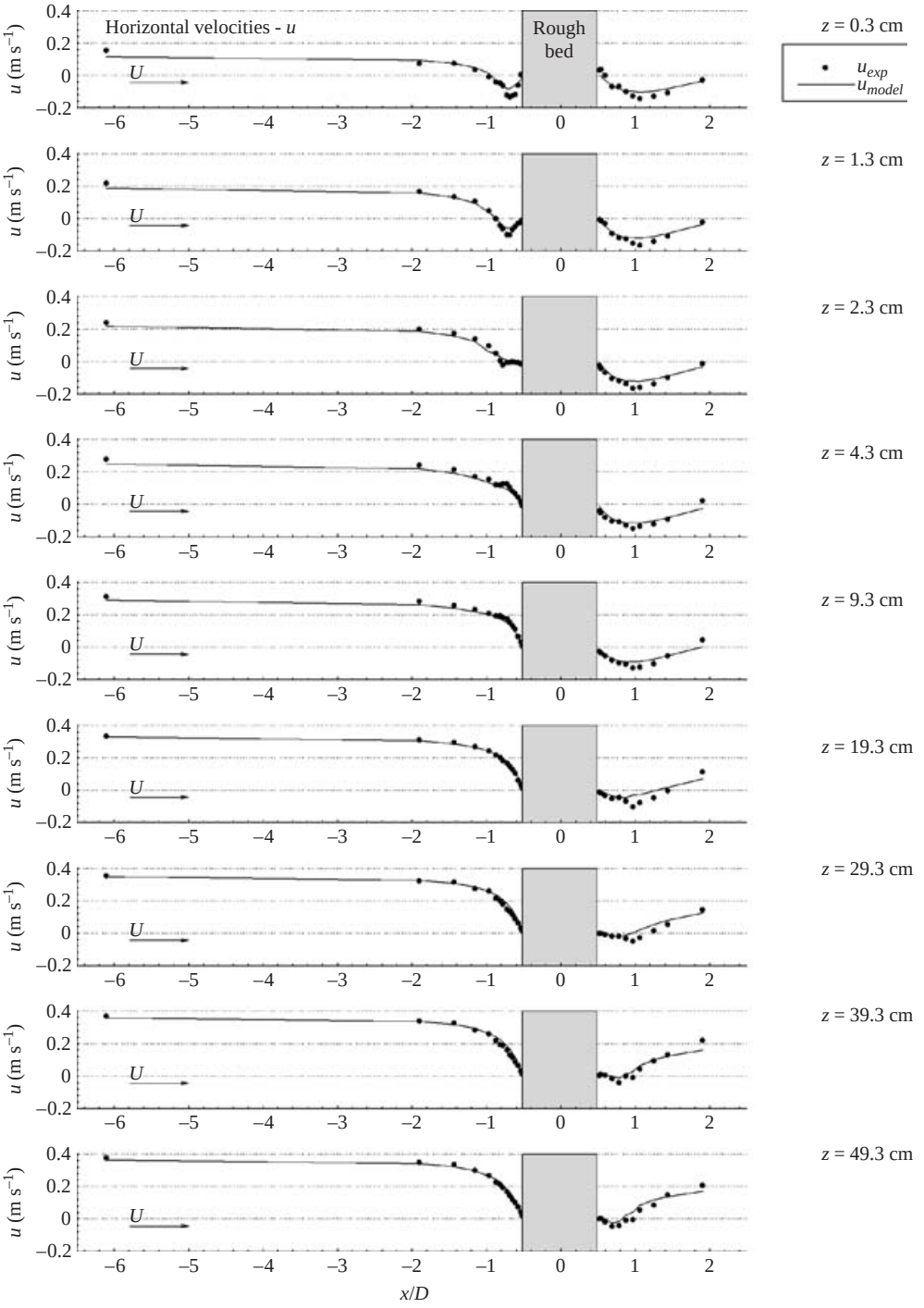

FIGURE 14. Horizontal velocity, u (m s^{-1}), in the plane of symmetry at different distances from the bed. Rough rigid bed (Test 2).

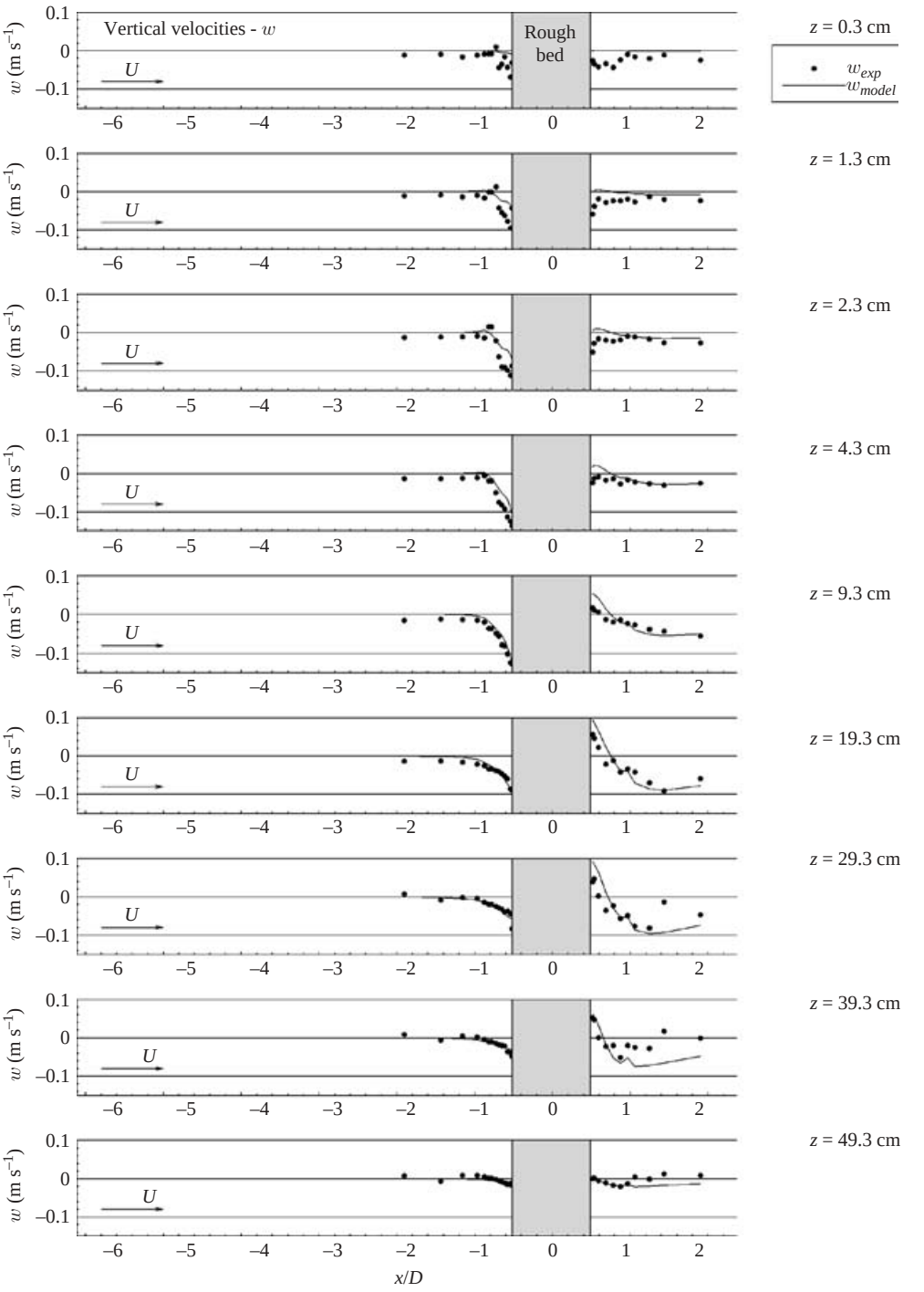

FIGURE 15. Vertical velocity, w (m s^{-1}), in the plane of symmetry at different distances from the bed. Rough rigid bed (Test 2).

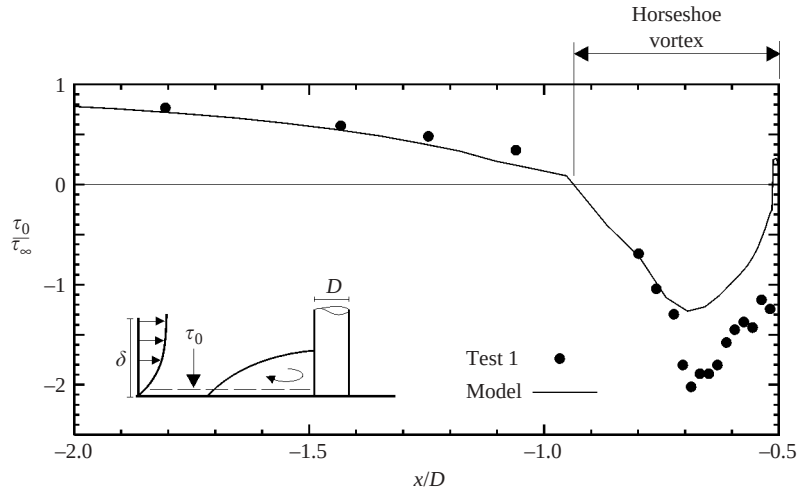

FIGURE 16. Bed shear stress amplification along the symmetry line upstream of the pile. Comparison with Test 1.

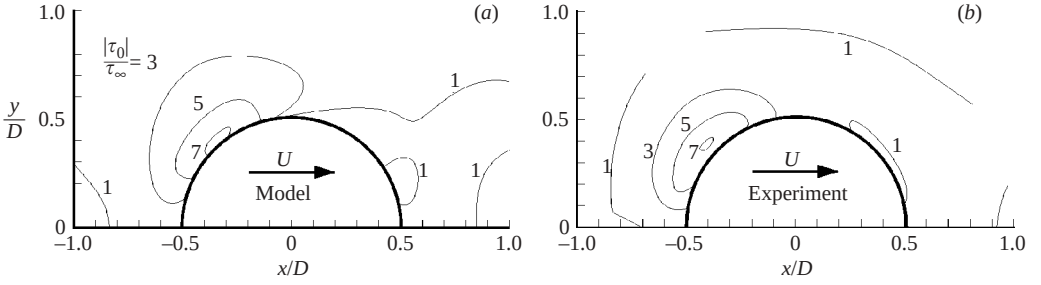

FIGURE 17. Bed shear stress amplification. (*a*) Model results. (*b*) Experiment (Hjorth 1975).

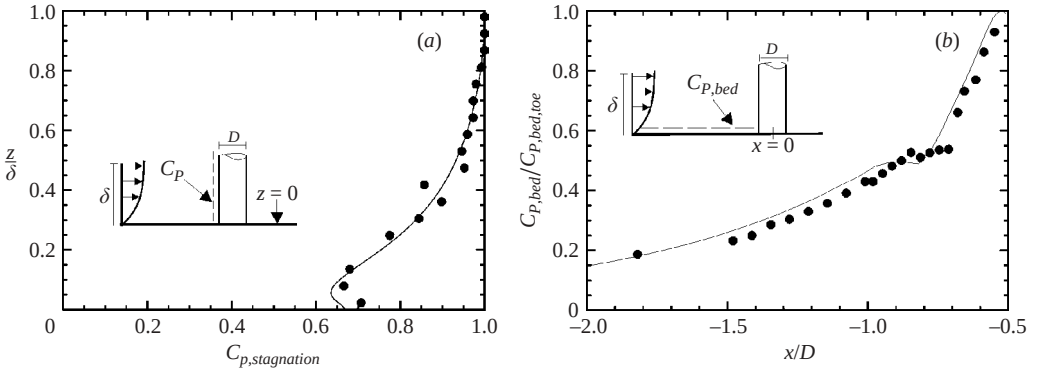

FIGURE 18. Pressure coefficient, C_p, upstream of the pile; ●, experimental data (Dargahi 1989) and —, model simulations. (*a*) C_p across the depth at the upstream edge of the pile. (*b*) C_p at the bed along the upstream symmetry line. Note: in (*b*) the pressure coefficient is normalized by the pressure coefficient at the toe of the pile ($x/D = -0.5$).

cylinder. The difference between the surface elevation in front and at the side edge of the cylinder is as much as $\Delta h = 5.2$ cm (see panels $\Theta = 0°$ and $\Theta = 90°$ in figure 19*b*). This difference and therefore the induced pressure gradient generates a strong down

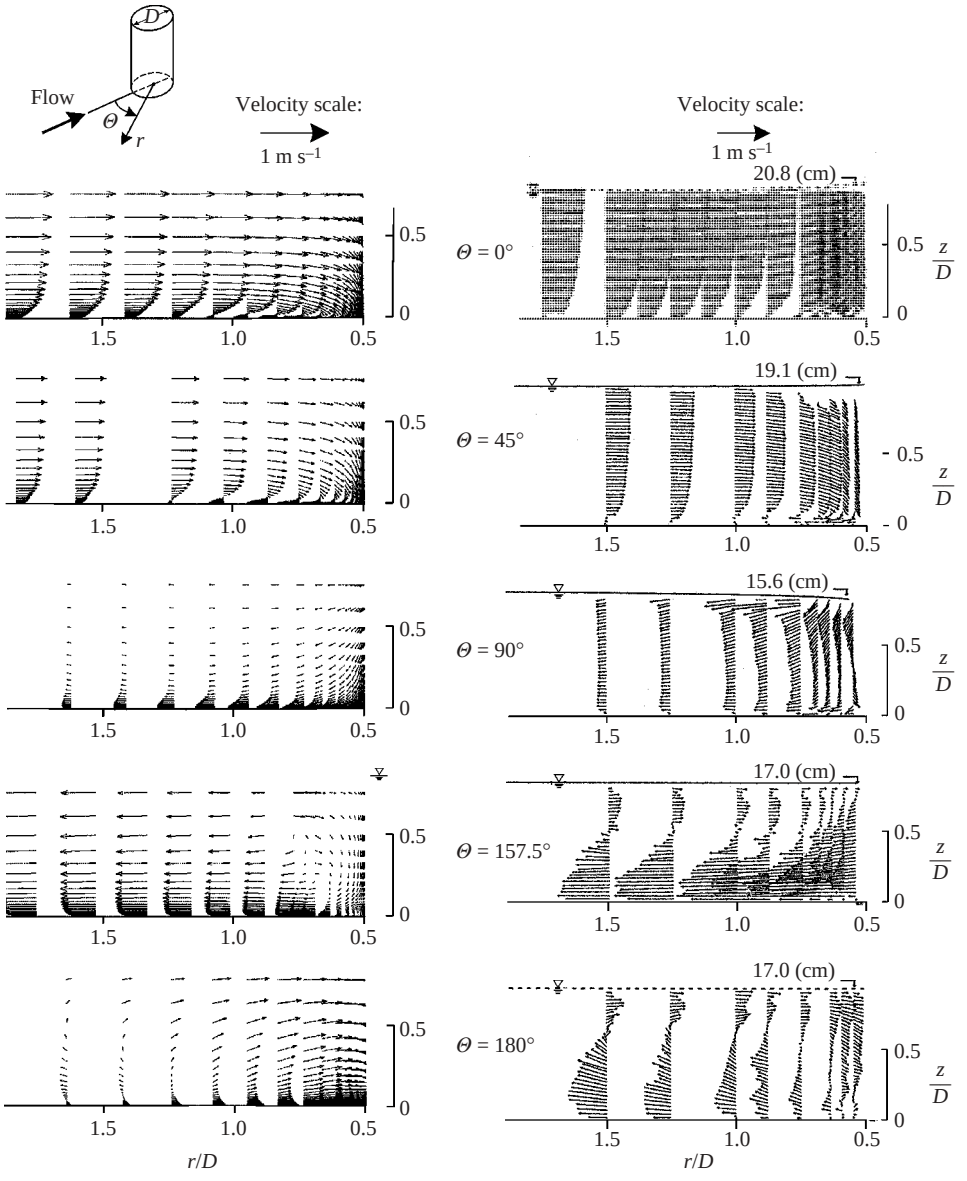

FIGURE 19. Velocity vector diagram in radial planes. (*a*) Model. (*b*) Experiments (Graf & Yulistiyanto 1998).

flow with a very strong component of flow velocity in the radial direction, as observed in figure 19(*b*) at $\Theta = 90°$, $\Theta = 157.5°$ and $\Theta = 180°$. As the numerical model cannot handle the free surface, the strong radial component of the flow observed in Graf & Yulistiyanto's experiment cannot be captured.

The previously described process is mainly controlled by the Froude number, Fr (equation (44)). The larger the value of Fr, the more pronounced the effect. In Graf & Yulistiyanto's experiment, $Fr = 0.5$. To observe the Froude-number effect in the laboratory, a supplementary experiment was carried out. Two tests were conducted in this supplementary experiment: one with $Fr = 0.5$ and the other with $Fr = 0.2$,

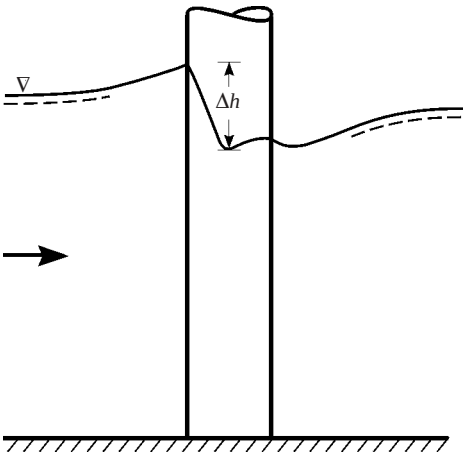

FIGURE 20. Schematic description of free-surface for high Froude numbers.

a relatively small Froude number to facilitate comparison between the high- and low-Froude-number cases. The test conditions were as follows: the water depth was $h = 26.1$ cm, the mean flow velocity $V = 30.0\,\mathrm{cm\,s^{-1}}$ for the $Fr = 0.2$ test and $V = 79.5\,\mathrm{cm\,s^{-1}}$ for the $Fr = 0.5$ test, the pile diameter $D = 31$ cm, the flume width was 2 m, and the bed was smooth. The horizontal component of the velocity was measured, using a micro propeller which was aligned with the flow direction at the measuring point. The direction of the flow at the measuring point was measured electronically, using a thin (1 mm thick) wing of area $1\,\mathrm{cm} \times 3\,\mathrm{cm}$. The radial component of the velocity was then calculated and plotted as a function of the vertical distance from the bed at different radial angles. Figure 21 displays the results for only two radial angles ($\Theta = 157.5^\circ$ and $\Theta = 180^\circ$) for reasons of space. The difference in the water level between the front and side edges of the cylinder was $\Delta h = 6.5$ cm for the $Fr = 0.5$ test and only $\Delta h = 1$ cm for the $Fr = 0.2$ test. Comparison of the velocity profiles between the two cases clearly shows that while the velocity profiles for $Fr = 0.2$ resemble the velocity distributions of figure 19(a) (no Fr number effect), the velocity profiles for $Fr = 0.5$ resemble the velocity profiles of figure 19(b), revealing the Froude-number effect on the flow field in the vicinity of the cylinder.

It may be noted that the Froude number of the present rigid-bed tests ($Fr = 0.14$, table 2), that of Hjorth's test (1975) ($Fr = 0.21$) and that of Dargahi's test ($Fr = 0.19$) are so small that the Froude-number effect was practically non-existent in these studies, and therefore the present numerical results and the experiments are in agreement.

The difference in the surface elevation between the front and side edges of the cylinder Δh may, to a first approximation, be written as $\Delta h/h = Fr^2/2$ for small Froude numbers. Using this relation, it can be seen that $\Delta h/h < O(0.02)$, a 'head' difference small enough not to cause any significant flow in the radial direction (practically no Froude-number effect) when $Fr < O(0.2)$. (For large Froude numbers, the quantity $\Delta h/h$ may be expected to be a function of not only the Froude number but also h/D.) At this juncture, it may be noted that the Froude number in most practical cases (except mountainous streams) is very small, certainly smaller than $O(0.2)$, and therefore the present numerical model (without the free surface 'facility') can be used with no serious implications.

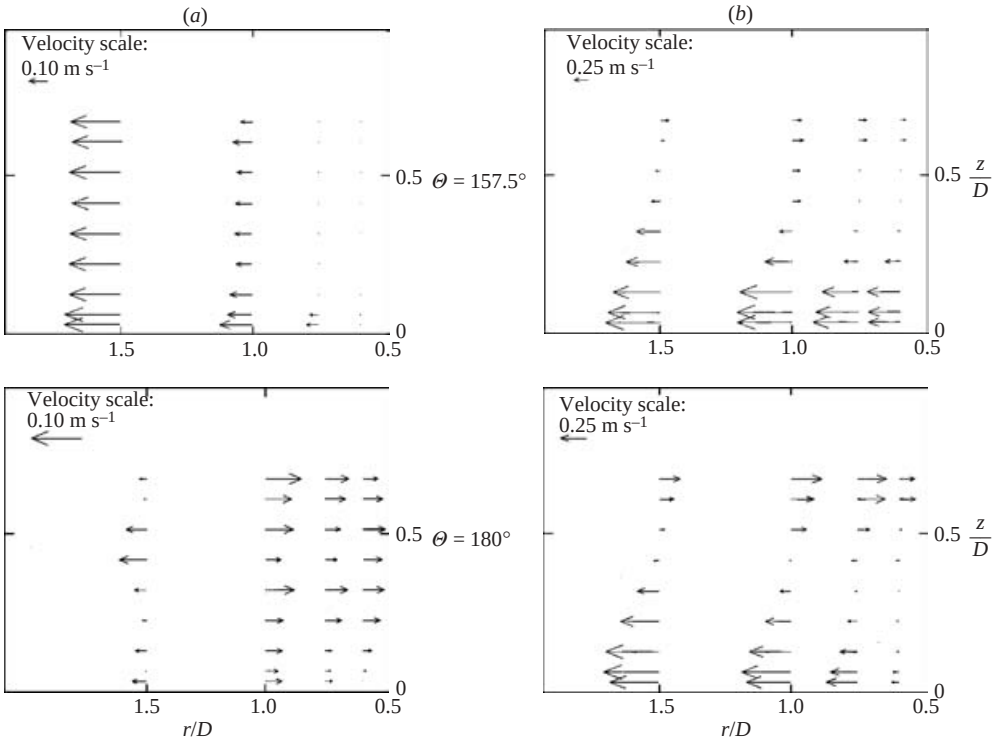

FIGURE 21. Effect of Froude number on the horizontal component of velocity in radial planes. Experiments (*a*) $Fr = 0.2$ and (*b*) $Fr = 0.5$.

From the preceding paragraphs, we can conclude that the present model captures well the mean properties of the flow around a circular pile, provided that the Froude number is small enough, and therefore the present model can be used for studying flow processes around the pile (such as the horseshoe vortex, the lee wake and the amplification of the bed shear stress) in such situations. The remainder of § 5 will focus on the latter.

5.2. *Horseshoe vortex*

The horseshoe vortex is caused by the rotation in the incoming flow; the boundary layer on the bed upstream of the pile undergoes a three-dimensional separation (along the dashed line, *S*, in figure 1) under the influence of the adverse pressure gradient (figure 18*b*) induced by the presence of the pile. The separated boundary layer subsequently rolls up to form a spiral vortex (the horseshoe vortex) around the structure, which then trails off downstream (figure 1).

From dimensional grounds, the non-dimensional quantities describing the horseshoe vortex in front of a circular pile with a smooth bed depend mainly on the following parameters (Baker 1979),

$$\frac{\delta}{D},\ Re_D \text{ (or, alternatively, } Re_\delta), \tag{48}$$

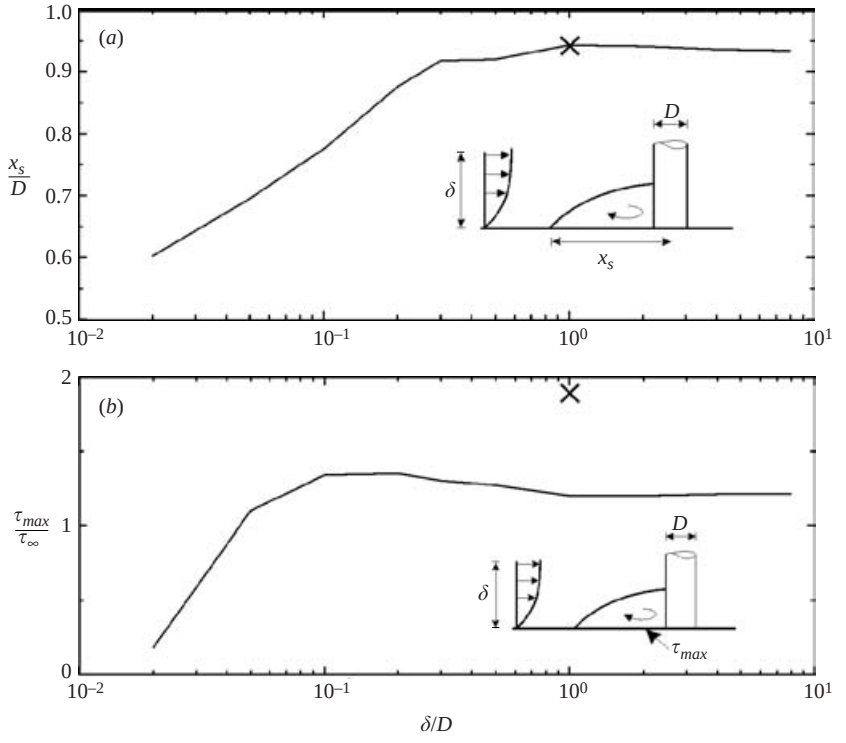

FIGURE 22. Influence of δ/D. Model results. Smooth, rigid-bed. $Re_D = 2 \times 10^5$. (*a*) Separation distance x_s/D as function of δ/D. Cross: present experiment (Test 1, from the bed shear stress measurements). (*b*) Maximum bed shear stress amplification under the horseshoe vortex on the upstream symmetry line. Cross: present experiment (Test 1).

in which δ/D is the ratio of the bed-boundary-layer thickness to the pile diameter, Re_D is the pile Reynolds number,

$$Re_D = \frac{UD}{\nu} \tag{49}$$

and Re_δ is the bed-boundary-layer-thickness Reynolds number

$$Re_\delta = \frac{U\delta}{\nu} \tag{50}$$

in which U is the velocity at the outer edge of the bed boundary layer (the free-stream velocity), figure 1. The latter definitions are slightly different from those in (42) and (43).

If the bed is rough, obviously the bed roughness (normalized by the pile diameter, k_s/D, or alternatively by the boundary-layer thickness, k_s/δ) should also influence the horseshoe vortex.

5.2.1. *Influence of the boundary-layer thickness*

The separation of the bed boundary layer (to form the horseshoe vortex) will be delayed if the boundary-layer-thickness-to-pile-diameter ratio, δ/D, is small (i.e. a more uniform velocity distribution in the incoming boundary layer, figure 1), presumably leading to a smaller-size horseshoe vortex. For very small values of δ/D, the boundary layer may not even separate, and hence no horseshoe vortex will be formed. Figure 22 shows the results of the present numerical simulations where the Reynolds number is kept constant at $Re_D = 2 \times 10^5$, and δ/D is changed.

In figure 22(*a*), the distance x_s is the length characterizing the size of the horseshoe vortex (see figure 1 and also the definition sketch in figure 22*a*). The following observations can be made from figure 22*a*:

(i) The figure clearly reveals the argument given in the preceding paragraph regarding the role of the boundary-layer-thickness-to-pile-diameter ratio: The smaller the value of δ/D, the smaller the size of the horseshoe vortex.

(ii) It may be inferred from figure 22(*a*) that $x_s/D \to 0.5$ (i.e. the horseshoe vortex ceases to exist) for very small values of δ/D (i.e. when $\delta/D < O(0.01)$).

(iii) Furthermore, it is seen from the figure that x_s/D attains a constant value, $x_s/D \simeq 0.95$, for large values of δ/D, namely, for $\delta/D > O(0.5)$. This is attributed to the finite 'penetration' distance of the adverse pressure gradient in front of the pile. From the potential-flow theory, it can easily be seen that this distance is $O(D)$. Therefore, the size of the horseshoe vortex should be expected to be $x_s = O(D)$ provided that δ/D is sufficiently large, as revealed by figure 22(*a*).

Finally, it may be noted that the data compiled by Sumer & Fredsøe (2002, p. 154), from Baker (1979), Sumer *et al.* (1997) and from their own experiments for Re_D covering the range $0.3 - 4 \times 10^4$ reveals the same kind of variation as in figure 22(*a*). (A direct comparison is not made here since the Reynolds number of the present simulation is outside the Reynolds-number range of the latter data.)

Figure 22(*b*) depicts the amplification of the maximum bed shear stress beneath the horseshoe vortex at the centreline, $\alpha_\tau = |\tau_0|/\tau_\infty$, plotted against δ/D. It is seen that the variation of α_τ with δ/D is similar to that in figure 22(*a*). This is because the bed shear stress underneath the horseshoe vortex is directly related to the size of the horseshoe vortex, x_s/D; the larger the horseshoe vortex, the larger the bed shear stress. Therefore the variation of α_τ should be similar to that of x_s/D.

5.2.2. *Influence of the Reynolds number*

Figure 23(*a*) displays the variation of the size of horseshoe-vortex, x_s/D, with the Reynolds number, obtained from the present numerical simulations where the boundary-layer-thickness-to-pile-diameter ratio is kept constant, at $\delta/D = 8$, and Re_D is changed.

Figure 23(*a*) indicates that (i) x_s/D increases with increasing Re_D when $Re_D < 500$ while (ii) it decreases with increasing Re_D when $Re_D > 500$.

This is interpreted as follows.

First of all, $Re_D = 500$ corresponds to the critical Reynolds number where the so-called primary oscillations in the horseshoe vortex (the oscillations of the separated flow system) first emerge (Baker 1991). Baker, from his experiments, concludes that this critical condition is reached when $Re_D(\delta^*/D)^{0.5} = 800$. For laminar conditions, taking $\delta^* \simeq \frac{1}{3}\delta$, (Schlichting 1979, p. 28), the Reynolds number corresponding to this critical condition is found to be $Re_D = 500$, meaning that $Re_D < 500$ therefore corresponds to the case of a separating laminar boundary layer while $Re_D > 500$ corresponds to the case of a separating turbulent boundary layer at the bed to form the horseshoe vortex.

Now, in the former case ($Re_D < 500$), the boundary-layer separation will be delayed if the Reynolds number is relatively smaller (i.e. relatively larger viscosity). This is because the boundary layer will 'face' larger resistance to separation and therefore the separation will be delayed, leading to a horseshoe vortex with relatively smaller size. (For very small Reynolds numbers, the boundary layer may not even separate, meaning that the horseshoe vortex may not even form). In conclusion, for $Re_D < 500$, the size of the horseshoe vortex decreases with decreasing Re_D, as revealed by figure 23(*a*).

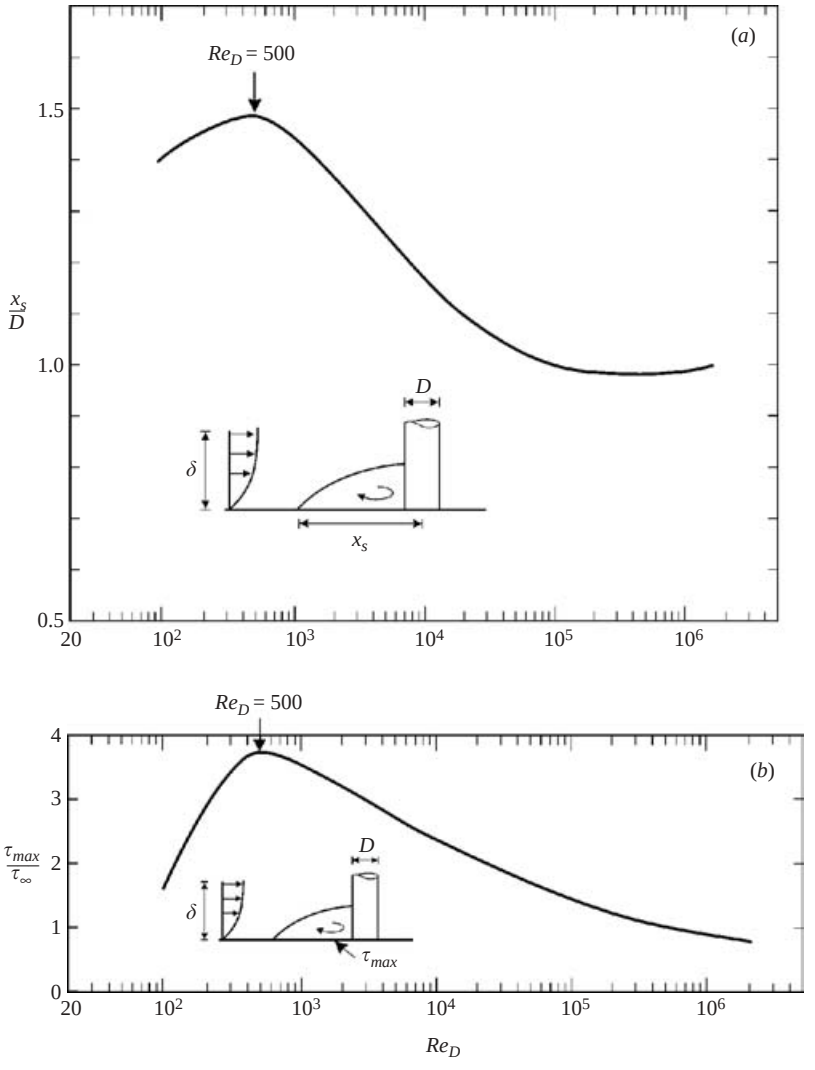

FIGURE 23. Influence of the pile Reynolds number Re_D. Model results. Smooth rigid-bed. $\delta/D = 8$. (*a*) Separation distance x_s/D. (*b*) Maximum bed shear stress amplification under the horseshoe vortex on the upstream symmetry line.

In the case of the separating turbulent boundary layer ($Re_D > 500$), the role of the Reynolds number is reversed, i.e. the size of the horseshoe vortex is decreased with increasing Reynolds number. This is due to the increased momentum exchange between the layers of fluid in the separating turbulent boundary layer (and therefore due to the delay in the boundary-layer separation) with increasing Reynolds number, a process similar to that experienced in the transition to turbulence at the separation point in the case of flow around a circular cylinder (Sumer & Fredsøe 1997, p. 12).

It may be noted that the numerical simulations made in the present study for very small Reynolds numbers covering $Re_D = 20 - 50$ showed that no separation occurred for $Re_D \leqslant 20$, while a 'separation eddy' formed at the bed in front of the pile for the range $30 \leqslant Re_D \leqslant 50$. In this latter case, the boundary layer first separates at

$x/D = (-1.3)$–(-1.45) and then reattaches the bed at $x/D = (-1.0)$–(-0.75) (and therefore no horseshoe vortex is generated), as Re_D is increased from 30 to 50.

The pile Reynolds number has also a significant influence on the strength of the horseshoe vortex. Figure 23(*b*) shows the amplification of the maximum bed shear stress beneath the horseshoe vortex, $\alpha_\tau = |\tau_0|/\tau_\infty$, plotted against Re_D. The observed variation of α_τ can be explained in terms of the variation of x_s/D with Re_D, i.e. similar to figure 23(*a*). As mentioned previously in conjunction with the previous figure, the Reynolds number $Re_D = 500$ (where the behaviour of the variation of α_τ changes) marks the point where the horseshoe vortex flow undergoes transition to turbulence for the tested value of δ/D, namely $\delta/D = 8$.

5.2.3. *Influence of the bed roughness*

Similar calculations were carried out for rough beds with $D/k_s = O(1) - O(10^3)$ and $Re_D = 2 \times 10^3$, 2×10^4, 2×10^5 and 10^6. The results (not shown here for reasons of space) indicate that the variations with D/k_s are not very extensive; x_s/D varies only by about 15 % and $\alpha_\tau = |\tau_0|/\tau_\infty$ only by 35 % when D/k_s is increased by a factor of 100. Nevertheless, the results show that there is a slight trend that x_s/D decreases with decreasing D/k_s (or, alternatively, with increasing roughness). This may be explained in the same way as in figure 23(*a*); namely, the larger the roughness, the larger the amount of turbulence put into the main body of the flow, and therefore the longer the delay in the boundary-layer separation. Hence, x_s/D should decrease with increasing bed roughness (or alternatively, with decreasing D/k_s). A slight decrease in $\alpha_\tau = |\tau_0|/\tau_\infty$ with decreasing D/k_s for $D/k_s \lesssim 10$ also can be explained in the same way.

5.3. *Lee-wake flow*

The lee-wake vortices are caused by the rotation in the boundary layer over the surface of the pile. The shear layers emanating from the side edges of the pile roll up to form these vortices in the lee wake of the pile (figure 1). The flow in the lee wake is unsteady for pile Reynolds number $Re_D > 40$ (see e.g. Sumer & Fredsøe 1997). The lee-wake flow is dependent mainly on Re_D. In the case of a rough pile, the relative roughness, k_s/D, emerges as an additional parameter. Here, k_s = the roughness of the pile surface.

Figure 24 depicts a sequence of velocity vector and streamline plots at the horizontal plane $z/\delta = 0.5$, obtained from the unsteady solution of the present model, during one half period of vortex shedding. Figure 25, on the other hand, presents a sequence of similar pictures at a horizontal plane very close to the bed, at $z/\delta = 0.025$, again during one half period of vortex shedding. The Reynolds number in these simulations was $Re_D = 4.6 \times 10^4$ and $\delta/D = 2$.

(i) From figures 24 and 25, the unsteady behaviour of the wake is evident.

(ii) Furthermore, figure 25 indicates the presence of the horseshoe vortex.

(iii) It can be seen from figure 25 that the unsteady component of the flow regarding the horseshoe vortex is essentially insignificant.

In the previously described steady-state solutions of the present flow model, the unsteady component of the flow is suppressed in the iteration procedure of the numerical simulations, as described in § 2.1. In this connection, an interesting question is: How does the steady solution compare with that obtained by time averaging of the unsteady solution (the time averaging taken over one vortex-shedding period). Figure 26(*a*) shows the contour plot of the bed shear stress obtained from the steady solution, while figure 26(*b*) shows that of the time-averaged bed shear stress from the unsteady simulation.

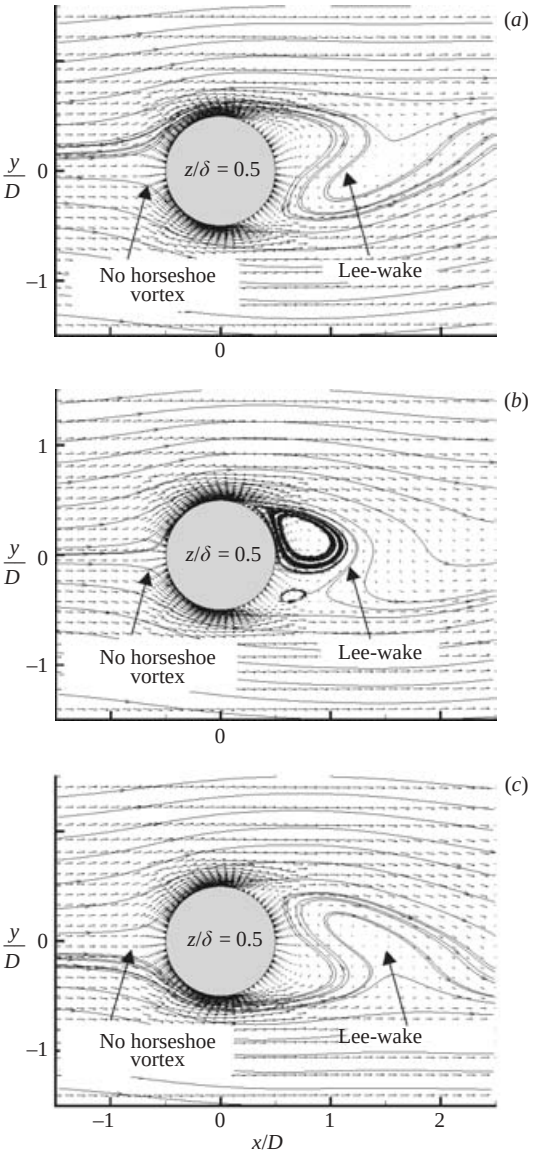

FIGURE 24. Velocity vectors and streamlines for unsteady flow simulation during one half period of vortex shedding. Smooth bed; $V = 46\,\mathrm{cm\,s^{-1}}$; $\delta = 20\,\mathrm{cm}$, $D = 10\,\mathrm{cm}$; $Re_D = 4.6 \times 10^4$. Horizontal cross-section at $z = 10\,\mathrm{cm}$ ($z/\delta = 0.5$).

As seen, the two plots are very much the same with two exceptions: (i) the area where there is high 'concentration' of flow is, to some degree, larger in the case of the steady-flow calculations than in the unsteady-flow calculations (e.g. the area with $|\tau_0|/\tau_\infty > 4$ extends to 100° in the former case, figure 26, while it extends to 90° in the latter, figure 26*b*); (ii) in the wake region, a slight difference is also observed.

The fact that the two solutions are rather close to each other would enable the large computational times to be reduced to manageable levels by conducting steady simulations of the flow for those problems where the oscillating components of the quantities are not very important (the reduction in the computational times can

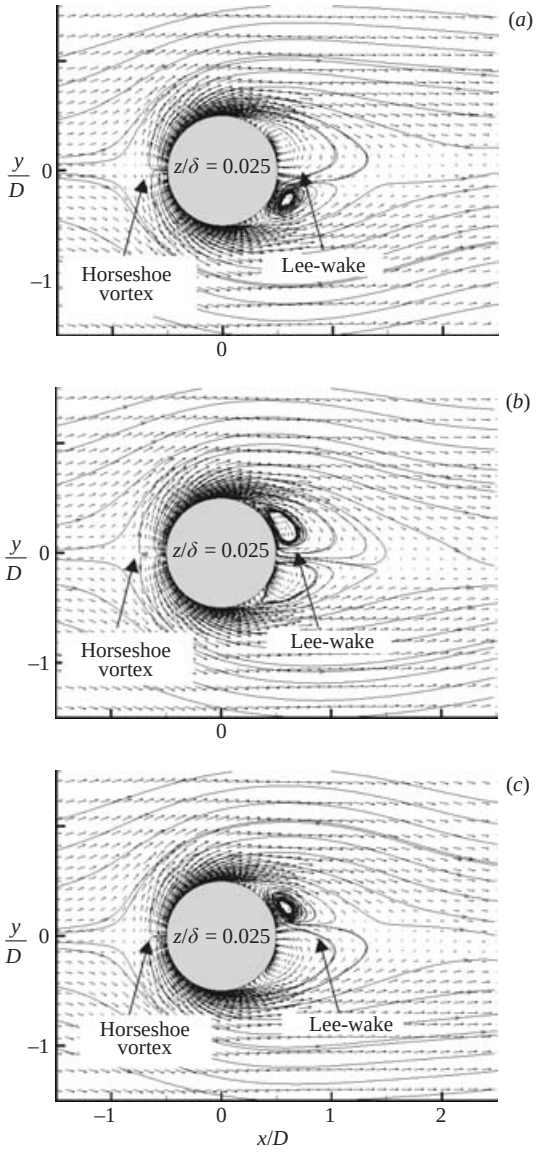

FIGURE 25. Velocity vectors and streamlines for unsteady flow simulation during one half period of vortex shedding. Smooth bed; $V = 46\,\mathrm{cm\,s^{-1}}$; $\delta = 20\,\mathrm{cm}$, $D = 10\,\mathrm{cm}$; $Re_D = 4.6 \times 10^4$. Horizontal cross-section at $z = 0.5\,\mathrm{cm}$ ($z/\delta = 0.025$).

be tremendous, by as much as an order of magnitude or even more). The steady-state flow calculations were used for the prediction of flow in connection with the numerical simulation of scour described in § 6. The implications of this approach for scour calculations will be discussed in § 6.

5.4. *Amplification of the bed shear stress*

The distribution of the bed shear stress has been discussed earlier in conjunction with (i) the horseshoe vortex (figures 22*b* and 23*b*) and (ii) the horseshoe vortex and unsteady solution (figure 26).

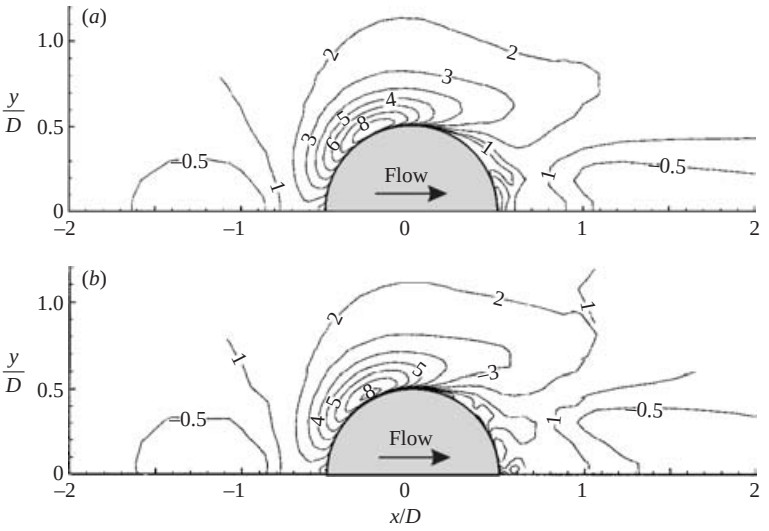

FIGURE 26. Contours of bed shear stress amplification. Smooth bed. $V = 46\,\mathrm{cm\,s^{-1}}$; $h(\sim\delta) = 20\,\mathrm{cm}$, $D = 10\,\mathrm{cm}$; $Re_D = 4.6 \times 10^4$. (*a*) Steady-state-flow simulation. (*b*) Time-averaged unsteady-flow simulation.

Figures 27–29 give the full picture of the bed shear stress in the form of contour plots, obtained from the present steady-state simulations. Figure 27 illustrates the variations as a function of δ/D, figure 28 as a function of Re_D, and figure 29 as a function of D/k_s.

The following conclusions can be drawn from figures 27–29.

(i) The figures (along with figures 17 and 26) show that the amplification of the bed shear stress is largest at the interval $\phi = 45°$–$70°$ in which ϕ is the angle measured from $-x$-axis. This large amplification is caused by the combined effect of the contraction of streamlines and the horseshoe vortex.

(ii) Figure 27 indicates that the maximum amplification of the bed shear stress gradually increases from $\alpha_\tau = |\tau_0|/\tau_\infty = 3$ to 5 when the boundary-layer-thickness-to-diameter ratio, δ/D, is increased from 0.02 to 2. This can be explained in terms of the horseshoe vortex. The horseshoe vortex increases in size as δ/D is increased from 0.02 to 2 (figure 22*a*). The larger the horseshoe vortex, the more 'violent' the flow adjacent to the pile towards the pile's side edges. Therefore, the amplification of the bed shear stress should be larger as δ/D is increased.

(iii) Figure 28 reveals an opposite effect, as the Reynolds number, Re_D, is increased gradually from 2×10^2 to 2×10^5. This behaviour can also be explained in terms of the horseshoe vortex. As seen from figure 23(*a*), the size of the horseshoe vortex does not change radically when Re_D is increased from 2×10^2 to 2×10^3. Therefore the maximum amplification is apparently the same for these two cases. However, when Re_D is increased further, the size of the horseshoe vortex decreases (figure 23*a*), and consequently the amplification of the bed shear stress will also decrease.

(iv) It may be noted that, although it is at best suggestive, this decrease in the amplification of the bed shear stress for very large Re_D, and similar results from figure 23*b*, along with those from figure 23(*a*), may help explain (albeit, partially) the observations that the scour depth, S/D, in the field is generally smaller than that measured in the laboratory (Melville & Coleman 2000, figure 6.29). Melville &

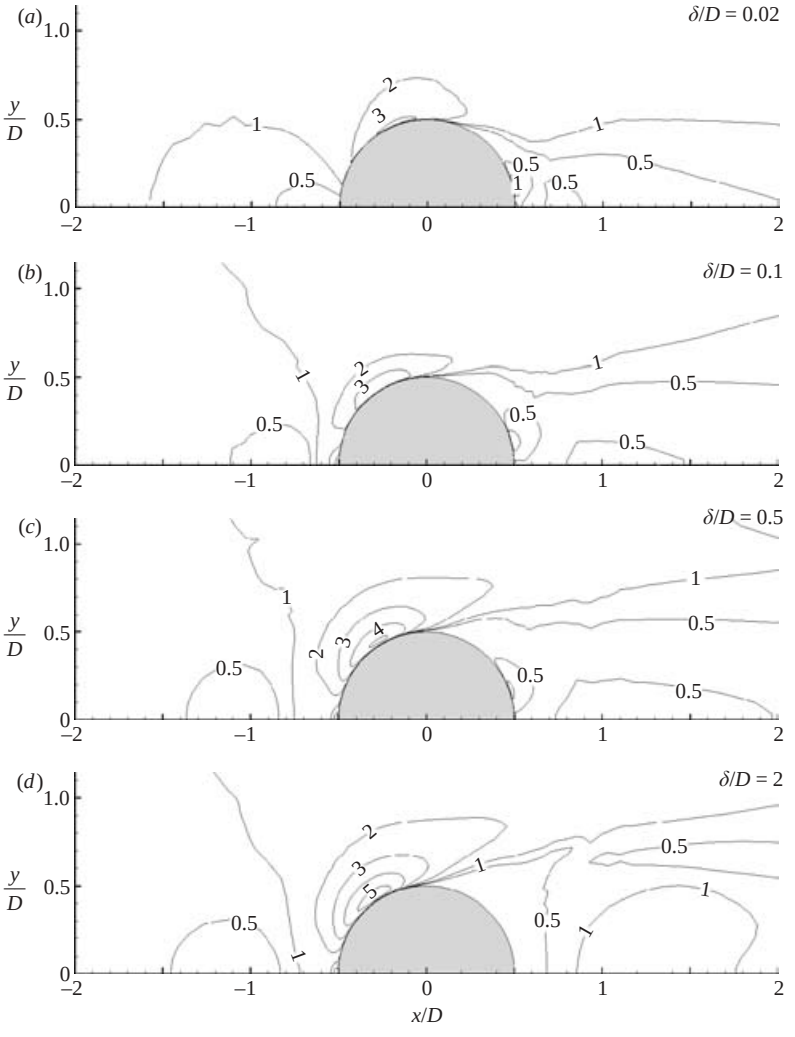

FIGURE 27. Contours of bed shear stress amplification for different values of δ/D. Model results. Smooth bed. $Re_D = 2 \times 10^5$.

Coleman list a number of other potential effects for the smaller scour depths observed in the field.

(v) The variation in $\alpha_\tau = |\tau_0|/\tau_\infty$ in figure 29 may be explained in the same way as in (iii) above.

6. Simulation of the scour process

6.1. *Experimental observation of the development of scour*

Figures 30 and 31 illustrate the way in which the scour develops in front and at the back of the pile, respectively, in the test described in § 4.2 (Test 3). As seen, the flow and scour processes are very violent in the beginning, but much less so at the end of the scour development. The scour hole emerges upstream of the pile owing to the increased extensive sediment transport under the horseshoe vortex. The eroded sediment is initially deposited at the back of the pile. As the process continues, the

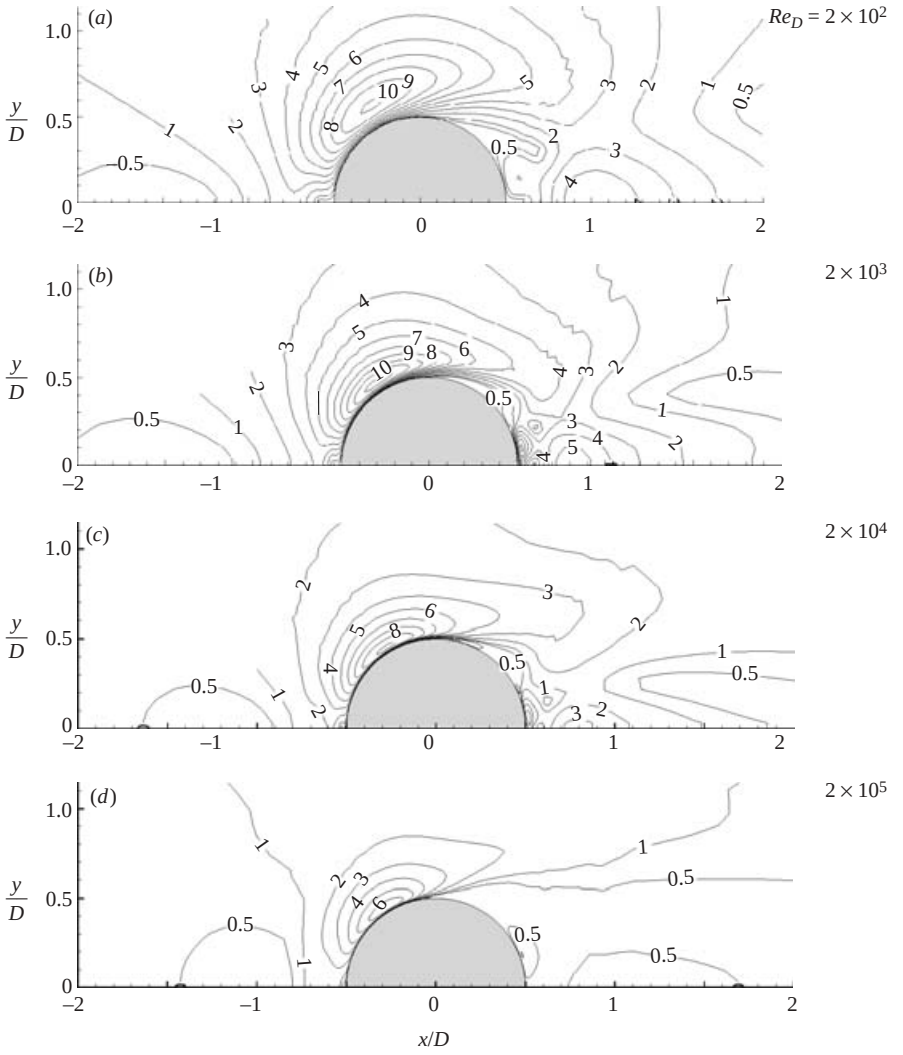

FIGURE 28. Contours of bed shear stress amplification for different values of Re_D. Model results. Smooth bed. $\delta/D = 8$.

scour depth upstream of the pile increases, and the scour hole works its way around to the downstream side of the pile. At the same time, the sand deposited at the back of the pile migrates downstream. The slope of the scour hole in the upstream part is equal to the angle of repose $\beta_r \simeq 32°$. It was observed in the test that, throughout the scour process, the scour depth upstream of the pile was larger than that downstream of the pile. As mentioned in § 4.2, the formation of migrating ripples outside the scour hole indicates that the scour in the test is in the live-bed regime (see figure 32, a photograph illustrating the scour hole attained in the equilibrium stage). Figure 32 shows that no ripples are present in the upstream part of the scour hole. As the ripples entered the scour hole from the upstream side, they 'disintegrate' and slide down the slope of the scour hole towards the pile and momentarily decrease the scour depth. As seen from figure 32, small ripples may develop in the downstream part of the scour hole.

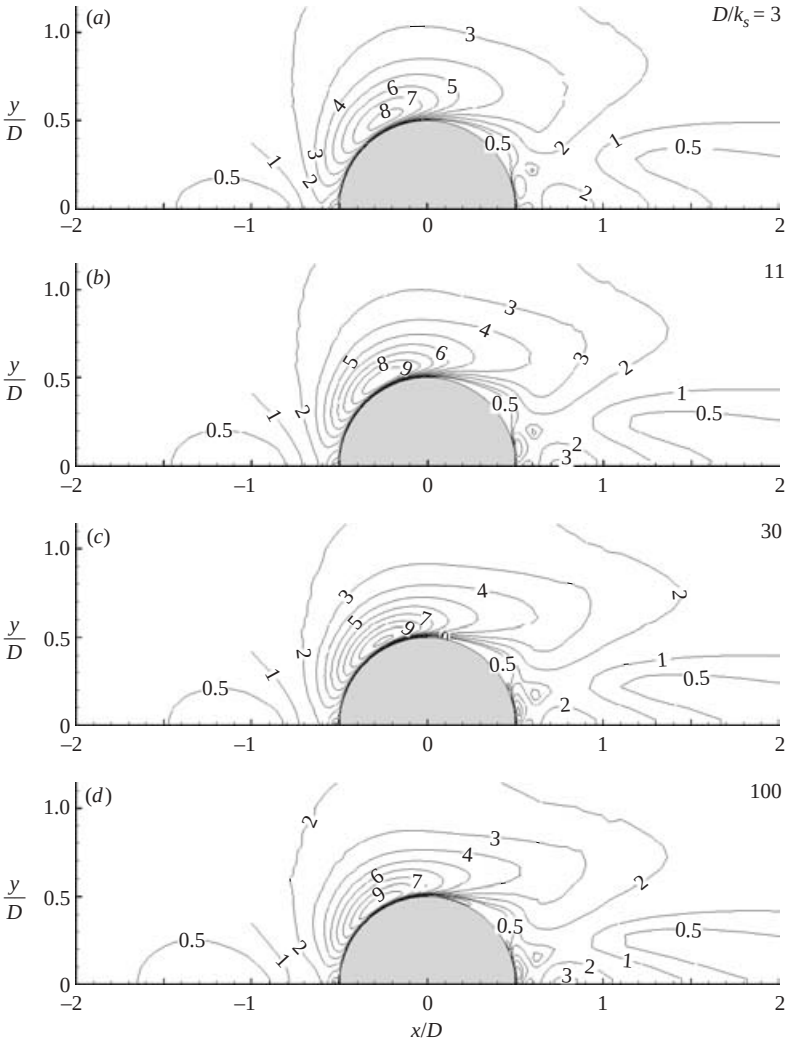

FIGURE 29. Contours of bed shear stress amplification for different values of bed roughness D/k_s. Model results. $\delta/D = 8$ and $Re_D = 2 \times 10^4$.

6.2. *Numerical simulation of scour*

As mentioned earlier, the steady-state flow calculations were used in the present simulation (vortex shedding was not resolved). This is because the computational time becomes prohibitively large for unsteady-flow calculations (§ 5.3). Clearly, there will be consequences of the steady-state approach. This will be discussed at the end of this section.

The water depth in the model was taken as $\delta = 20\,\text{cm}$, corresponding to the measured boundary-layer thickness in Test 3. The pile diameter was $D = 10\,\text{cm}$. The mean velocity was $V = 46\,\text{cm s}^{-1}$. $Re_D = 4.6 \times 10^4$. Based on the mean grain size $d_{50} = 0.26\,\text{mm}$, Nikuradse's equivalent sand roughness was $k_s \approx 2.5 \cdot d_{50} = 0.65\,\text{mm}$. The undisturbed Shields parameter in the scour simulation was $\theta = 0.11$, i.e. in the live bed regime. The ratio between the approach velocity and the critical velocity for initiation of sediment motion was $V/V_{cr} = 1.25$.

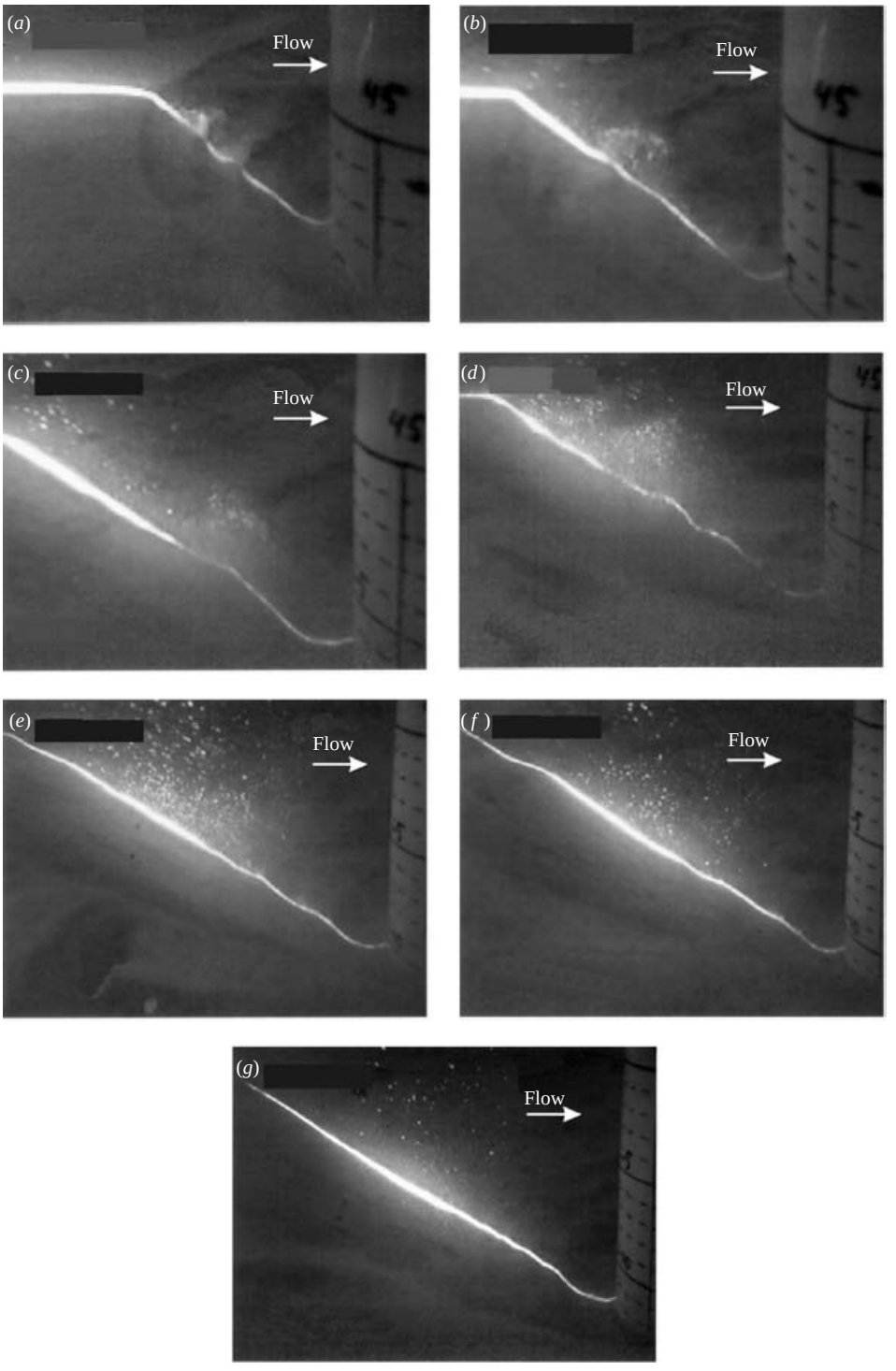

FIGURE 30. Visualization of flow and scour at the base of a circular pile in steady current. Test 3. Upstream symmetry line. (*a*) $t = 1$ min; (*b*) 2 min; (*c*) 5 min; (*d*) 10 min; (*e*) 30 min; (*f*) 1 h; (*g*) 2 h.

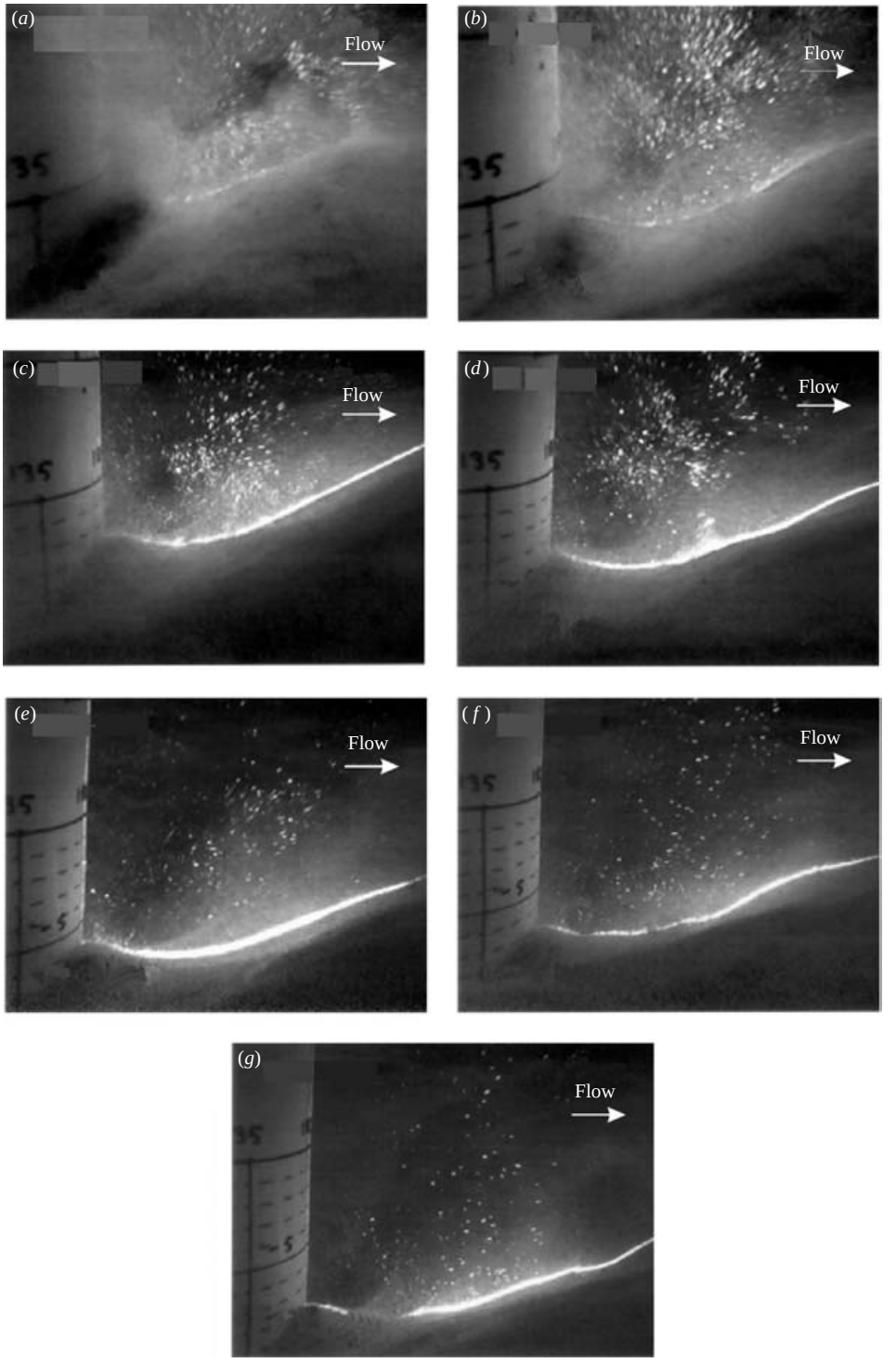

FIGURE 31. Visualization of flow and scour at the base of a circular pile in steady current. Test 3. Downstream symmetry line. (*a*) $t = 1$ min; (*b*) 2 min; (*c*) 5 min; (*d*) 10 min; (*e*) 30 min; (*f*) 1 h; (*g*) 2 h.

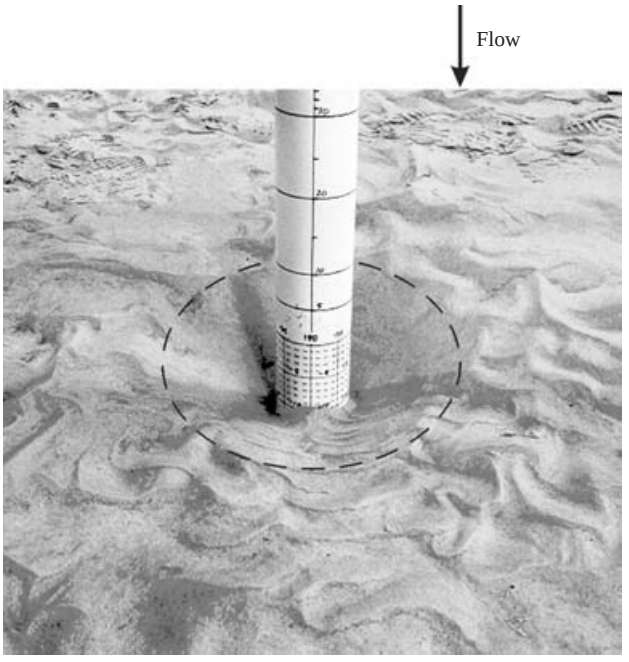

FIGURE 32. Equilibrium scour hole in Test 3.

The bed ripples were resolved in the simulations. To trigger the development of ripples, a perturbation was applied to the prescribed bed roughness in the first 30 s of the simulation. This perturbation was maintained at the first three rows of the computational cells at the inlet to ensure the continued migration of ripples into the computational domain. The sediment transport description in the present model was based on uniform-size sand, i.e. the sediment gradation was $\sigma_g = 1.0$ (cf. $\sigma_g = 1.5$ of Test 3, see § 4.2). The effect of sediment gradation was therefore not reproduced in the simulation. This may have an effect on the scour depth, as will be discussed later in this section.

(It may be noted that the present numerical-simulation exercise was done earlier in Roulund (2000). However, in the calculations, the first term in the bracket in (25) was inadvertently taken as $\sqrt{1-(\sin^2\alpha\tan^2\beta)/\mu_s^2}$ rather than $\cos\beta\sqrt{1-(\sin^2\alpha\tan^2\beta)/\mu_s^2}$, and therefore the results reported in Roulund *et al.* (2000) and later partly reported in Roulund *et al.* (2002) regarding the scour process are, to some extent, in error. The numerical equilibrium scour depth found in Roulund (2000) was 20 % larger at the upstream side and 17 % larger at the downstream side of the pile than the corresponding values measured in the experiment).

Figure 33 shows a sequence of pictures, illustrating the time evolution of the scour hole obtained in the present simulation.

From the simulation results, all the topographic bed features observed in Test 3 are captured:

(i) The semi-circular shape (in plan view) of the upstream part of the scour hole with a slope equal to the angle of repose.

(ii) The formation of a 'bar' downstream of the pile (the deposited sand), and its downstream migration.

(iii) The formation of a gentler slope of the downstream side of the scour hole.

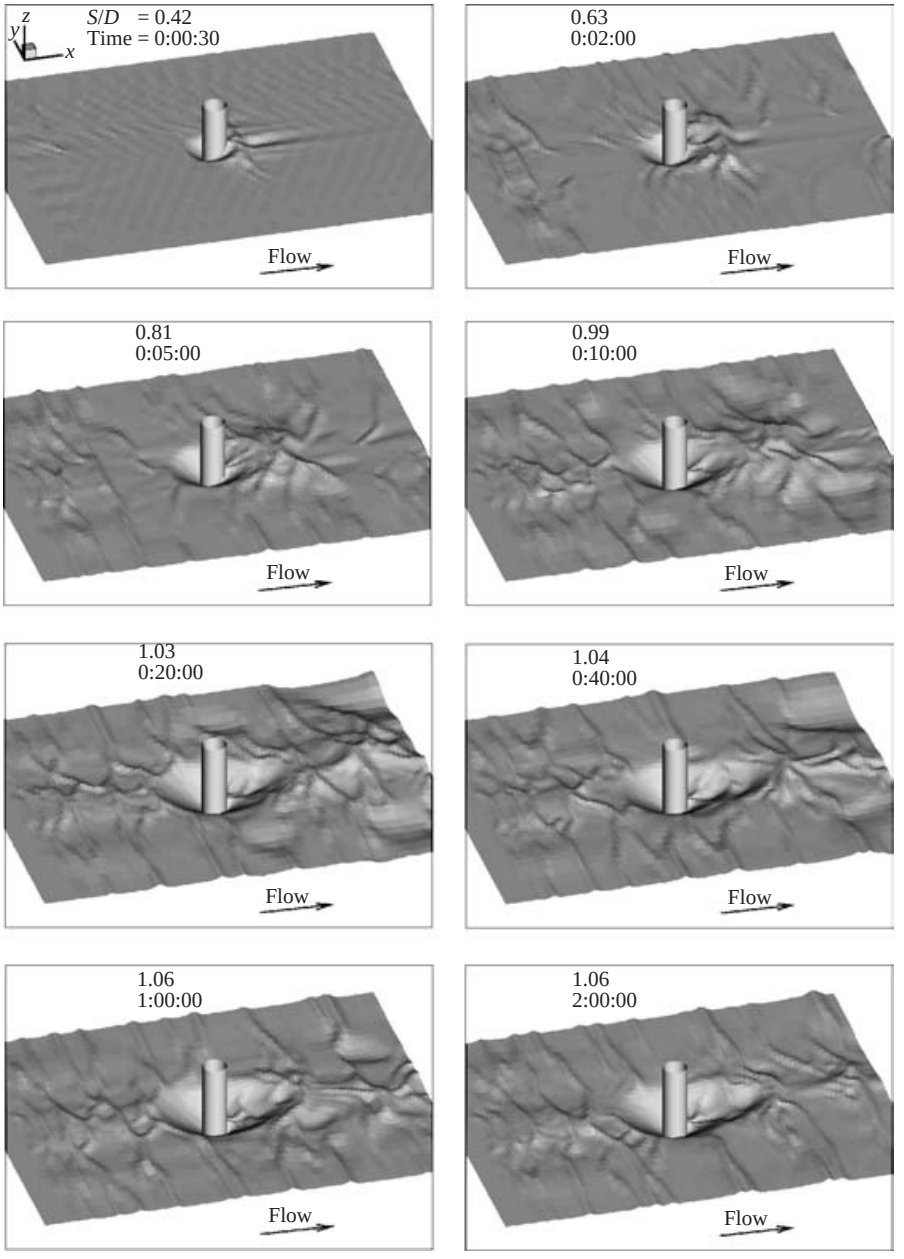

FIGURE 33. Scour development. Model results. $V = 46\,\mathrm{cm\,s^{-1}}$; $D = 10\,\mathrm{cm}$; $\delta = 20\,\mathrm{cm}$; $k_s = 0.7\,\mathrm{mm}$; $Re_D = 4.6 \times 10^4$; $d_{50} = 0.26\,\mathrm{mm}$; $\sigma_g = 1.0$. Time = h:min:s. Maximum scour depth indicated in the panels.

(iv) The formation and migration of ripples at the downstream side of the scour hole.

Figure 34 shows the time development of the scour depth at the upstream side (figure 34*a*) and at the downstream side (figure 34*b*) of the pile. Figure 35, on the other hand, shows the scour-hole profiles along the upstream–downstream symmetry line.

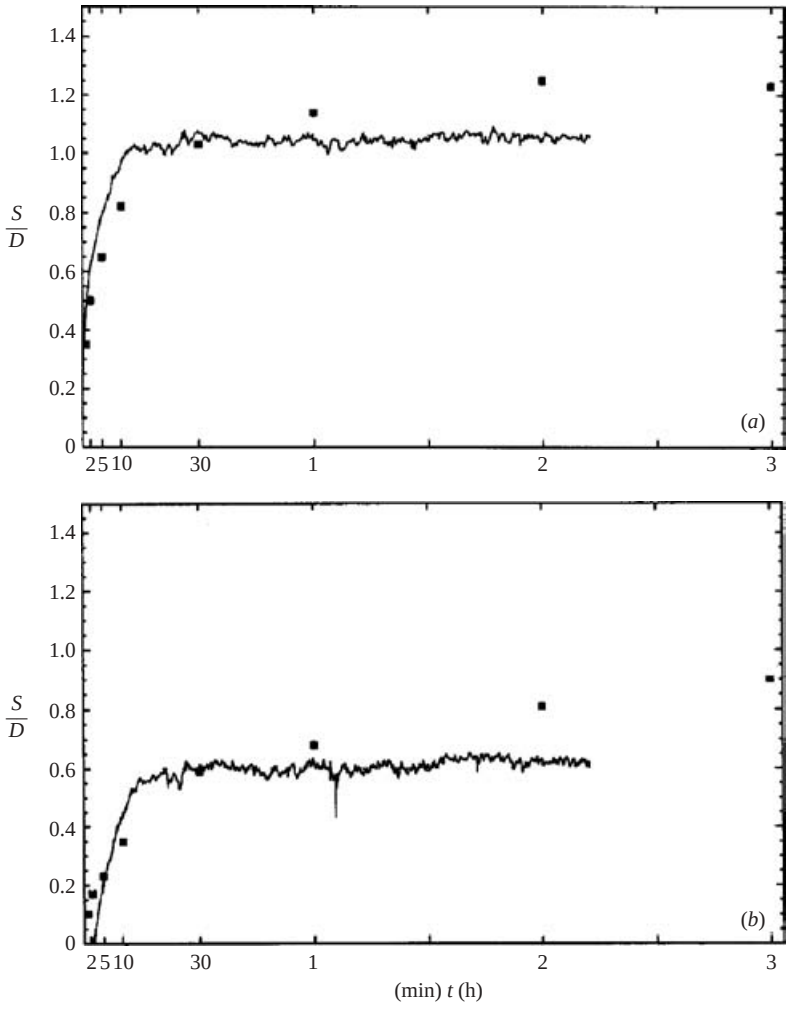

FIGURE 34. Scour development. Data points: experiment (Test 3). Continuous line: numerical simulation. (*a*) Scour depth at upstream edge of pile. (*b*) Scour depth at downstream edge of pile.

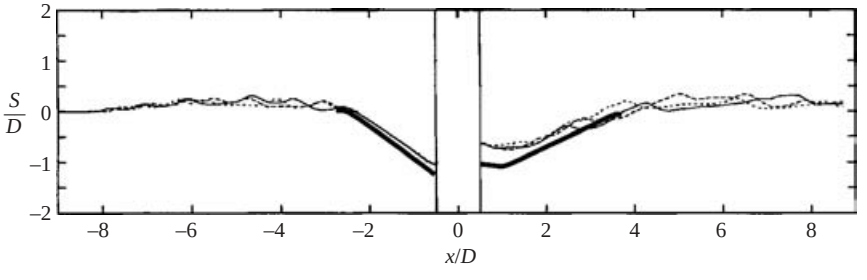

FIGURE 35. Equilibrium scour profile along the length of the longitudinal symmetry axis. Thick line: experiment. Thin lines: numerical simulation results (dotted line, $t = 1$ h; dashed line, $t = 1.33$ h; Full line, $t = 2$ h).

(i) The equilibrium scour depth is apparently underpredicted by the numerical simulation, by about 15 % for the upstream scour depth and by about 30 % for the downstream scour depth (figure 34).

(ii) At the initial stage of the scour process, the scour depth is predicted well by the numerical simulation at the upstream edge of the pile (figure 34*a*) while it is underpredicted at the downstream edge (figure 34*b*). The latter discrepancy (up to a few minutes from the start) is due to suspended load process (figure 31*a–c*). The suspended load process is not covered in the model, and therefore the model scour depth remains rather small during this stage (figure 34*b*).

(iii) The scour profile predicted by the numerical simulation at the upstream side of the scour hole agrees well with the experiment (figure 35). The downstream profile, however, deviates from the experimental profile by about 30 %, consistent with the result in conjunction with the downstream scour depth (figure 34*b*), indicating that scour is somewhat underpredicted over an area of the downstream scour hole extending from the pile to $x/D = 3$.

The difference (although not radically large) between the numerical simulation and the experiment observed in figures 34 and 35 may, to a large extent, be attributed to the unsteady effects, the effects which are not accounted for in the present steady-state-flow model, namely (i) the unsteady flow due to vortex shedding in the lee wake of the pile and (ii) that due to the horseshoe vortex in front of the pile. Measurements show that turbulence (representing the 'fluctuating components' of the horseshoe-vortex and lee-wake vortex flows) can be considerable (Sumer *et al.* 1997; Graf & Yulistiyanto 1998). Although Sumer *et al.* (1988) showed that the lee-wake vortices may contribute to downstream scour substantially in the case of a pipeline, to our knowledge, no experimental study is available investigating the effect of turbulence on scour around a pile. From the study of Sumer *et al.* (1988), it is inferred that the end effect of the unsteady-flow calculation will be to increase the predicted scour depth downstream of the pile. The same is also true for the upstream part of the scour hole. However, a scour-simulation exercise with the unsteady-flow calculation is unfortunately not within reach at the present time (as mentioned previously, even with the steady-state flow calculations, a single run for the scour calculation requires 2.5 months on an Alpha 21264 workstation, § 3.3). Another effect to explain the difference between the numerical result and the experiment may be the uncertainty in determining the boundary-layer thickness in the experiment. The water depth in the model was taken as $\delta = 20$ cm, corresponding to the measured boundary-layer thickness in Test 3, as mentioned earlier. When plotted in linear scale, the velocity profile in figure 9 indicates that there may be an uncertainty in the boundary-layer thickness, δ; this is towards values slightly larger than the selected value (not larger than $\delta = 25$ cm, however). When $\delta = 25$ cm, this boundary-layer thickness (the flow depth) would give a scour depth approximately 10 % larger than the predicted one, using the empirical information on the variation of the scour depth with the flow-depth-to-pile-diameter ratio, δ/D, given in Sumer & Fredsøe (2002, figure 3.28). This may account for some of the discrepancy between the model and the experiment. However, in particular, the 30 % difference between the model and the experiment downstream of the pile cannot be accounted for in terms of the flow depth alone.

As a final note regarding the unsteady effects, the suspended-load process exhibited in figure 31 is due to the vortex shedding where the vortices act like 'cyclones' or 'tornadoes' to pick up the sediment from the bottom and transport it in the downstream direction, similar to the description given in Sumer, Christiansen & Fredsøe (1992, p. 28). Therefore, in a possible suspended-load simulation, the following

components must be present in the model: (i) the suspended-load sediment transport; and (ii) the unsteady component of the flow (i.e. the vortex shedding).

Scour around a circular pile in steady current has been investigated extensively in the laboratory in the past three decades. Important contributions are Melville & Raudkivi (1977), Raudkivi & Ettema (1977, 1983), Raudkivi (1986), Melville & Sutherland (1988), Melville & Raudkivi (1996), Ettema, Melville & Barkdoll (1998); see also Raudkivi (1998). This work has shown that the scour depth is influenced by various factors the most important of which are: (i) The boundary-layer-depth-to-pile-size ratio, δ/D (the scour depth, S/D, increases with increasing δ/D); (ii) the Shields parameter, or alternatively V/V_c in which V is the mean flow velocity and V_c is the mean flow velocity corresponding to the critical condition at the bed (S/D generally increases with increasing V/V_c, except that it experiences a slight dip after the scour regime changes from the clear-water scour to the live-bed scour); (iii) the gradation of the sediment, σ_g (S/D decreases with increasing σ_g); (iv) the pile-diameter-to-sediment-size ratio, D/d (S/D increases with increasing D/d); (v) the Reynolds number, Re_D; and (vi) The Froude number, Fr. The reported range of the equilibrium scour depth, S/D, is $O(1–2.5)$ for the live-bed scour, the actual value depending on the previously mentioned parameters.

Baker (1986) (see also Melville & Coleman 2000, p. 493) reports experimental data for the equilibrium scour depth as a function of the sediment gradation σ_g and the velocity ratio V/V_c.

The present numerical result is compared with Baker's result corresponding to $V/V_c = 1.25$ and $\sigma_g = 1.3$ (for the sediment with a size distribution closest to uniform) in the following table. Note that although the Froude number for the numerical test is $Fr(= V/\sqrt{gh}) = 0.33$, the simulated flow will behave like that with $Fr \to 0$ because the model does not have the free surface (for this reason, no value is entered in the following table for Fr).

	δ/D	V/V_c	σ_g	D/d_{50}	Re_D	Fr	S/D
Baker's (1986) experiment	> 4	1.25	1.3	75	$\sim 10^5$	~ 0.2	1.9
Present numerical simulation	2	1.25	1.0	385	4.6×10^4	–	1.1

Now, the data compiled by Melville & Sutherland (1988) indicates that S/D becomes independent of the pile-diameter-to-sediment-size ratio, D/d_{50}, when $D/d_{50} \gtrsim 40$. Since this ratio both in Baker's experiment and in the present numerical simulation is larger than 40, the parameter D/d_{50} does not influence the variation of S/D. Furthermore, the Reynolds number, Re_D, of the present numerical work and that of Baker's experiments are not radically different. The difference in the Reynolds numbers would translate into a small difference in the size of the horseshoe vortex (a difference less than 5 %, see figure 23*a*) and therefore can be disregarded. Finally, the Froude number of the experiment ($Fr = 0.2$) and that of the numerical model ($Fr \to 0$) are so small that the effect of the Froude number also can be disregarded.

Baker's (1986) data indicate that the normalized equilibrium scour depth S/D (for the sediment with a size distribution closest to uniform, namely for $\sigma_g = 1.3$) is $S/D = 1.9$ (see the above table). The present numerical simulation (for sediment with a uniform size distribution, $\sigma_g = 1$) predicts this value as $S/D = 1.1$, a value 42 % smaller than Baker's measurement. This discrepancy is due partly to the effect of turbulence (described in detail in the preceding paragraphs) and partly to the relatively small

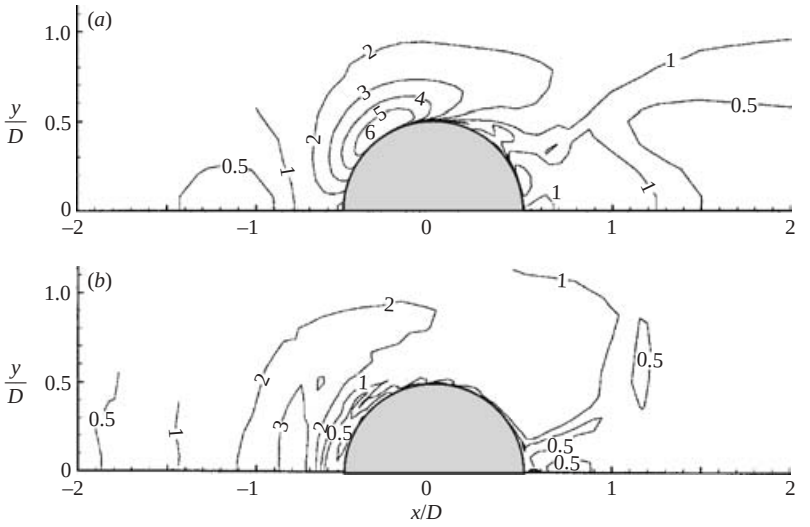

FIGURE 36. Bed shear stress amplification. Model results. (*a*) Initial plane bed. (*b*) Equilibrium scoured bed. $Re_D = 4.6 \times 10^4$.

value of the boundary-layer-depth-to-pile-diameter ratio in the present simulation, namely $\delta/D = 2$ versus $\delta/D > 4$ in Baker's experiments (see Melville & Sutherland 1988, p. 196 and Sumer & Fredsøe 2002, p. 180 for the influence of the boundary-layer thickness on the scour depth).

Finally, figure 36 shows the bed shear stress amplification for the initial plane bed and that for the equilibrium scoured bed in the simulation. The bed shear stress amplification of the equilibrium stage is reduced considerably, apparently from a maximum value of $\alpha_\tau = |\tau_0|/\tau_\infty = 6$ (figure 36*a*) to $\alpha_\tau = 3$ (figure 36*b*). However, note that the bed shear stress in the scour hole over a crescent-shaped area from $x/D \simeq -1.5$ up to $x/D \simeq +0.5$ is still larger than that outside the scour hole (figure 36*b*). In the case of the scoured bed (figure 36*b*; see also figure 35), the horseshoe vortex forms inside the scour hole in front of the pile extending across $-2 \lessapprox x/D < -0.5$. Just in front of the pile, the bed shear stress underneath the horseshoe vortex is obviously zero. It begins to pick up with the distance from the pile, and apparently reaches a value as high as $\alpha_\tau = 3$ at $x/D = -0.7$. This high value of the bed shear stress is linked to the concentration of the flow in the horseshoe vortex at this location. However, as the flow in the horseshoe vortex continues towards the separation line at the upstream edge of the scour hole, the flow velocity (and therefore the bed shear stress) will decrease. Although there is a significant amount of amplification of the bed shear stress in the scour hole, the sediment transport 'uphill' owing to this bed shear stress will be balanced by the sand slide, leading to a scour hole geometry which is in equilibrium. Melville & Raudkivi (1977) obtained estimates of mean bed shear stress from the mean velocity measurements for three cases, namely on the initial flat bed, intermediate scour hole and the final equilibrium scour hole. The bed shear stress measurements in the two cases of scour holes are particularly interesting. Although no direct comparison between the present numerical findings and Melville & Raudkivi's results could be made, Melville & Raudkivi's results show that there exists a crescent-shaped area inside the scour hole in front of the pile where the bed shear stress is larger than the undisturbed bed shear stress, in exactly the same fashion as in the present numerical results (figure 36*b*).

7. Conclusions

(i) A three-dimensional hydrodynamic model, EllipSys3D, incorporated with the k–ω turbulence model was chosen to simulate the flow around a vertical circular pile exposed to a steady current. The model, tested and validated against the experimental data (from the present study and from others), was used to study the horseshoe vortex and lee-wake flow processes. The influence of three parameters, the boundary-layer thickness, the Reynolds number and the bed roughness, on the horseshoe vortex was investigated. Likewise, the influence of the unsteady solution on the previously mentioned flow processes was also investigated.

(ii) The numerical results show that the size of the horseshoe vortex and the bed shear stress under the horseshoe vortex increase with increasing boundary-layer-thickness-to-pile-diameter ratio, δ/D, until the latter quantity reaches a certain value. Beyond that value, these quantities do not vary with increasing δ/D. The results also show that the horseshoe vortex ceases to exist when δ/D is very small. For $Re_D = 2 \times 10^5$, it was found that the horseshoe vortex does not exist when $\delta/D < O(0.01)$.

(iii) The influence of the Reynolds number, Re_D, on the horseshoe vortex was also found to be significant. The results indicate that the size of the horseshoe vortex and the bed shear stress under the horseshoe vortex vary significantly with Re_D. It was found that the value of Re_D at which these quantities attain their maximum values coincides with the critical value of the Reynolds number associated with the transition to turbulence in the horseshoe vortex. In the laminar regime, the size of the horseshoe vortex and the bed shear stress were found to increase with increasing Re_D, while, in the turbulent regime, the converse is true.

(iv) The influence of the bed roughness on the horseshoe vortex was found to be not very extensive.

(v) The time-averaged bed shear stress obtained from the unsteady solution was found to be rather close to that obtained from the steady solution of the model, a result that would enable the large computational times for unsteady simulations to be reduced greatly (by as much as an order of magnitude) by conducting steady simulations of the flow. This is particularly important for numerical computations of scour processes where the computational time would be prohibitively large otherwise.

(vi) The bed shear stress calculations conducted for various values of the governing parameters (namely, δ/D, Re_D and the bed roughness) show that (*a*) the amplification of the bed shear stress near the pile is largest at $\phi = 45°$–$70°$ (in which ϕ is the angle measured from the main flow direction), and (*b*) the amplification can reach very large values (as large as $O(10)$), depending on the previously mentioned parameters.

(vii) The flow model (with steady solution) was coupled with a morphologic model to calculate scour around a vertical circular pile exposed to a steady current.

(viii) The results show that the present numerical simulation captures all the main features of the scour process.

(ix) It was found that the equilibrium scour depth obtained from the simulation agrees reasonably well with the experiment for scour upstream of the pile (the computed scour depth being 15 % smaller than the scour depth obtained in the experiment) while some differences (as much as 30 % underpredicted) are observed for scour downstream of the pile. This was attributed to the steady-state flow model where the unsteady effects (the fluctuating components of horseshoe vortex and lee-wake vortex flows) are not accounted for.

(x) The calculations also show that the amplification of the bed shear stress around the pile in the equilibrium state of scour is reduced considerably with respect to that experienced at the initial stage where the bed is plane.

This study was partially funded by the Commission of the European Communities, Directorate-General XII for Science, Research and Development Program Marine Science and Technology (MAST III) Contract no. MAS3-CT97-0097, Scour Around Coastal Structures (SCARCOST), FP5 specific program 'Energy, Environment and Sustainable Development' Contract No. EVK3-CT-2000-00038, Liquefaction Around Marine Structures LIMAS and Framework Program 'Computational Hydrodynamics' of the Danish Technical Research Council (STVF).

Martin Dixen, conducted the supplementary tests described in § 5.10.

REFERENCES

Allen, J. R. L. 1985 *Physical Sedimentology*. Allen & Unwin.

Baker, C. J. 1979 The laminar horseshoe vortex. *J. Fluid Mech.* **95**, 347–367.

Baker, C. J. 1991 The oscillation of horseshoe vortex systems. *Trans. ASME* I: *J. Fluids Engng* **113**, 489–495.

Baker, R. A. 1986 Local scour at bridge piers in non-uniform sediment. Thesis presented to the University of Auckland, New Zealand, in partial fulfilment of the requirements for the degree of Master of Philosophy.

Breusers, H. N. C., Nicollet, G. & Shen, H. W. 1977 Local scour around cylindrical piers. *J. Hydraul. Res.* **15**, 211–252.

Breusers, H. N. C. & Raudkivi, A. J. 1991 *Scouring*. A. A. Balkema, Rotterdam.

Briley, W. R. & McDonald, H. 1981 Computation of three-dimensional horseshoe vortex flow using the Navier–Stokes equations. *Proc. 7th Intl Conf. on Numerical Methods in Fluid Dynamics, Stanford, CA* (ed W. C. Reynolds & R. W. MacCormack), Lecture Notes in Physics, vol. 141, pp. 91–98. Springer.

Cebeci, T. & Chang, K. C. 1978 Calculation of incompressible rough-wall boundary-layer flows. *AIAA J.* **16**, 730–735.

Chen, H.-M. 2002 Numerical simulation of scour around complex piers in cohesive soil. *Proc. First Intl Conf. on Scour of Foundations, ICSF-1, Texas A&M University, College Station, Texas, USA, 17–20, November 2002*, vol. 1, pp. 14–33.

Dargahi, B. 1982 Local scour around bridge piers – A review of practice and theory. *Bull.* 114, Hydraulics Laboratory, Royal Institute of Technology, Stockholm, Sweden.

Dargahi, B. 1989 The turbulent flow around a circular cylinder. *Exps. Fluids* **8**, 1–12.

Deng, G. B. & Piquet, J. 1992 Navier–Stokes computations of horseshoe vortex flows. *Intl J. Numer. Meth. Fluids* **15**, 99–124.

Dey, S. 1997*a* Local scour at cylindrical piers, Part I: A review of developments of research. *Intl J. Sediment Res.* **12**, 23–46.

Dey, S. 1997*b* Local scour at cylindrical piers, Part II: Bibliography. *Intl J. Sediment Res.* **12**(3), 45–57.

Dey, S. 2003 Threshold of sediment motion on combined transverse and longitudinal sloping beds. *J. Hydraul. Res.* **41**, 405–415.

van Driest, E. R. 1956 On turbulent flow near a wall. *J. Aeronaut. Sci.* **23**, 1007–1011, 1036.

Einstein, H. A. & El Samni, E. A. 1949 Hydrodynamic forces on a rough wall. *Rev. Mod. Phys.* **21**, 520–524.

Engelund F. 1966 Hydraulic resistance of alluvial streams. *J. Hydraul. Div. ASCE*, (HY2) **92**, 315–326, Closure: 1967, (HY4) **93**, 287–296.

Engelund, F. & Fredsøe, J. 1976 A sediment transport model for straight alluvial channels. *Nordic Hydrol.* **7** 293–306.

Ettema, R., Melville, B. W. & Barkdoll, B. 1998 Scale effect in pier-scour experiments. *J. Hydraul. Engng ASCE* **124**, 639–642.

Fredsøe, J. & Deigaard, R. 1992 *Mechanics of Coastal Sediment Transport, Advanced Series on Ocean Engineering* 3. World Scientific, Singapore.

Graf, W. H. & Yulistiyantou, B. 1998 Experiments on flow around a cylinder; the velocity and vorticity fields. *J. Hydraul. Res.* **36**, 637–653.

Hanratty, T. J. & Campbell, J. A. 1983 Measurements of wall shear stress. In *Fluid Mechanics Measurements* (ed. R. J. Goldstein). Hemisphere.

Hjorth, P. 1975 Studies on the nature of local scour. *Bull. Ser.* A, no. 46, viii + 191 pp., Department of Water Resources Engineering, Lund Institute of Technology/University of Lund, Lund, Sweden.

Hoffmans, G. J. C. M. & Verheij, H. J. 1997 *Scour Manual.* A. A. Balkema, Rotterdam.

Issa, R. I. 1986 Solution of implicitly discretized fluid flow equations by operator splitting. *J. Comput. Phys.* **62**, 40–65.

Johansen, J., Sørensen, N. N., Michelsen, J. A. & Schreck S. 2002 Detached-eddy simulation of flow around the NREL Phase VI blade. *Wind Energy* **5**, 185–187.

Kwak, D., Rogers, S. E., Kaul, U. K. & Chang, J. L. C. 1986 A numerical study of incompressible juncture flows. *NASA TM* 88319, Ames Research Center, Moffet Field, CA 94035.

Lambe, T. W. & Whitman, R. V. 1969 *Soil Mechanics.* John Wiley.

Luque, R. F. 1974 Erosion and transport of bed sediment. Dissertation, Jrips Repro B.V.-Meppel.

Meland, N. & Norman, J. O. 1966 Transport velocities of single particles in bed-load motion. *Geografiska Annaler* **48**, A.

Melville, B. W. & Coleman, S. E. 2000 *Bridge Scour.* Water Resources, LLC, CO, USA, xxii + 550 p.

Melville, B. W. & Raudkivi, A. J. 1977 Flow characteristics in local scour at bridge piers. *J. Hydraul. Res.* **15**, 373–380.

Melville, B. W. & Raudkivi, A. J. 1996 Effects of foundation geometry on bridge pier scour. *J. Hydraul. Engng ASCE* **122**, 203–209.

Melville, B. W. & Sutherland, A. J. 1988 Design methods for local scour at bridge piers. *J. Hydraul. Engng ASCE* **114**, 1210–1226.

Menter, F. R. 1993 Zonal two equation k–ω turbulence models for aerodynamic flows. *AIAA Paper* 93-2906, *AIAA 24th Fluid Dynamic Conference, July 6–9, 1993, Orlando, Florida.*

Michelsen, J. A. 1992 Basis3D – a platform for development of multiblock PDE solvers. *Tech. Rep.* Dept of Fluid Mechanics, Technical University of Denmark, AFM 92-05, ISSN 0590-8809.

Nezu, I. 1977 Turbulent structure in open channel flows. PhD thesis, Kyoto University, Japan.

Olsen, N. R. B. & Kjellesvig, H. M. 1998 Three-dimensional numerical flow modelling for estimation of maximum local scour. *J. Hydraul. Res.* **36**, 579–590.

Olsen, N. R. B. & Melaaen, M. C. 1993 Three-dimensional calculation of scour around cylinders. *J. Hydraulic Engng ASCE* **119**, 1048–1054.

Patankar, S. V. 1980 *Numerical heat transfer and fluid flow.* Series in Computational Methods in Mechanics and Thermal Sciences. Taylor & Francis.

Raudkivi, A. J. 1986 Functional trends of scour at bridge piers. *J. Hydraul. Engng ASCE* **112**, 1–13.

Raudkivi, A. J. 1998 *Loose Boundary Hydraulics.* A. A. Balkema, Rotterdam.

Raudkivi, A. J. & Ettema, R. 1977 Effect of sediment gradation on clear water scour. *J. Hydraul. Engng ASCE* **103**, 1209–1213.

Raudkivi, A. J. & Ettema, R. 1983 Clear water scour at cylindrical piers. *J. Hydraul. Engng ASCE* **109**, 338–350.

Richardson, E. V. & Davies, S. R. 1995 *Evaluating Scour at Bridges.* 3rd edn. US Department of Transportation, HEC 18, FHWA-IP-90-017.

Richardson, J. E. & Panchang, V. G. 1998 Three-dimensional simulation of scour-inducing flow at bridge piers. *J. Hydraul. Engng ASCE* **124**, 530–540.

Rotta, J. C. 1962 Turbulent boundary layers in incompressible flows. In *Progress in Aeronautical Sc. – Boundary Layer Problems* (ed. A. Ferri, D. Küchhemann & L. H. G. Strene), pp. 1–220. Pergamon.

Roulund, A. 2000 Three-dimensional modelling of flow around a bottom-mounted pile and its application to scour. PhD thesis, Department of Hydrodynamics and Water Resources, Technical University of Denmark.

ROULUND, A., SUMER, B. M., FREDSØE, J. & MICHELSEN, J. 2002 3-D numerical modelling of flow and scour around a pile. *Proc. First Intl Conf. on Scour of Foundations, 17–20 November, 2002*, Texas A&M University, College Station, Texas, USA, vol. 2, pp. 795–809.

SCHLICHTING, H. 1979 *Boundary Layer Theory*, 7th edn. McGraw-Hill.

SHEN, W. Z., MICHELSEN, J. A. & SØRENSEN, J. N. 2001 An improved Rhie–Chow interpolation for unsteady flow computation. *AIAA J.* **39**, 2406–2409.

SHEN, W. Z., MICHELSEN, J. A. & SØRENSEN, J. N. 2004 A collocated grid finite volume method for aeroacoustic computations of low-speed flows. *J. Comput. Phys.* **196**, 348–366.

SHEN, W. Z., MICHELSEN, J. A., SØRENSEN, N. N. & SØRENSEN, J. N. 2003 An improved SIMPLEC method on collocated grids for steady and unsteady flow computations. *Numer. Heat Transfer* B **43**, pp. 1–19.

SØRENSEN, N. N. 1995 General purpose flow solver applied to flow over hills. PhD thesis, Risø National Laboratory, Roskilde, Denmark, Risø-R-827(EN).

SØRENSEN, N. N., MICHELSEN, J. A. & SCHRECK, S. 2002 Navier–Stokes predictions of the NREL phase VI rotor in the NASA Ames 80 ft × 120 ft wind tunnel. *Wind Energy* **5**, 151–169.

SPALDING, D. B. 1972 A novel finite-difference formulation for differential expressions both first and second order derivatives. *Intl J. Numer. Methods Engng* **4**, 551.

SUMER, B. M. 1984 Lift forces on moving particles near boundaries. *J. Hydraul. Engng ASCE* **110**, 1272–1279.

SUMER, B. M., ARNSKOV, M. M., CHRISTIANSEN, N. & JØRGENSEN, F. E. 1993 Two-component hot-film probe for measurements of wall shear stress. *Exps Fluids* **15**, 380–384.

SUMER, B. M., CHRISTIANSEN, N. & FREDSØE, J. 1997 Horseshoe vortex and vortex shedding around a vertical wall-mounted cylinder exposed to waves. *J. Fluid Mech.* **332**, 41–70.

SUMER, B. M., CHUA, L. H. C., CHENG, N.-S. & FREDSØE, J. 2003 The influence of turbulence on bedload sediment transport. *J. Hydraul. Engng ASCE* **129**(8), 585–596.

SUMER, B. M., COKGOR, S. & FREDSØE, J. 2001 Suction removal of sediment from between armour blocks. *J. Hydraul. Engng ASCE* **127**(4), 293–306.

SUMER, B. M. & FREDSØE, J. 1997 *Hydrodynamics Around Cylindrical Structures*. World Scientific.

SUMER, B. M. & FREDSØE, J. 2002 *The Mechanics of Scour in the Marine Environment*. World Scientific.

SUMER, B. M., FREDSØE, J. & CHRISTIANSEN, N. 1992 Scour around a vertical pile in waves. *J. Waterway Port Coastal Ocean Engng ASCE* **117**, 15–31.

SUMER, B. M., JENSEN, R., MAO, Y. & FREDSØE, J. 1988 The effect of lee-wake on scour below pipelines in current. *J. Waterway Port Coastal Ocean Engng ASCE* **114**, 599–614.

TSENG, M.-H., YEN, C.-L. & SONG, C. C. S. 2000 Computation of three-dimensional flow around square and circular piers. *Intl J. Numer. Methods Fluids* **34**, 207–227.

WHITEHOUSE, R. 1998 *Scour at Marine Structures*. Thomas Telford.

WILCOX, D. C. 1993 *Turbulence modelling for CFD*, 2nd edn. DCW Industries, La Cañada, California, USA.